

## Article

# Influence of NaAlO<sub>2</sub> Concentration on the Characteristics of Micro-Arc Oxidation Coating Fabricated on a ZK60 Magnesium Alloy

Shu-Fan Zhou<sup>1</sup>, Sheng Lu<sup>1</sup>, Wei-Gang Lv<sup>1</sup>, Ze-Xin Wang<sup>1,\*</sup>, Dubovyy Oleksandr<sup>2</sup>, Jun-Jie Gu<sup>1</sup>, Jin-Wei Zhang<sup>1</sup> and Liang-Yu Chen<sup>1,\*</sup> 

<sup>1</sup> School of Material Science and Technology, Jiangsu University of Science and Technology, Zhenjiang 212003, China; 221110601232@stu.just.edu.cn (S.-F.Z.); lusheng\_ktz@just.edu.cn (S.L.); wzxlwg@126.com (W.-G.L.); 211210601209@stu.just.edu.cn (J.-J.G.); zjw\_mumu@126.com (J.-W.Z.)

<sup>2</sup> Department of Material Science and Technology of Metals, Admiral Makarov National University of Shipbuilding Institute, 54025 Nikolaev, Ukraine; oleksandr.dubovyy@nuos.edu.ua

\* Correspondence: wangzexin@just.edu.cn (Z.-X.W.); lychen@just.edu.cn (L.-Y.C.)

**Abstract:** This study investigated the impact of NaAlO<sub>2</sub> concentration in electrolytic solutions on micro-arc oxidation (MAO) coatings, focusing on their surface quality enhancement and corrosion resistance improvement. The surface morphology and microstructure of these coatings were assessed using scanning electron microscopy. Mechanical properties, such as hardness and wear resistance of MAO coatings, were tested. The hardness of the 6 g/L group was 411.2 HV. X-ray photoelectron spectroscopy examinations showed that MgAl<sub>2</sub>O<sub>4</sub>, CaMgP<sub>2</sub>O<sub>7</sub>, and MgSiO<sub>4</sub> were the phases in the MAO coating. Antibacterial assessments were performed to evaluate the influence of NaAlO<sub>2</sub> concentration, and the antibacterial rate of the 6 g/L group reached 97.08%. The hydrophilicity of the coatings was determined using water contact angle measurements, wherein the water contact angle of the 6 g/L was the lowest, at 58.25°. Corrosion resistance was evaluated with an electrochemical workstation. The findings revealed that the MAO coatings prepared with a NaAlO<sub>2</sub> concentration of 6 g/L exhibited superior uniformity with fewer defects, enhanced corrosion resistance, and increased adhesive strength compared to other concentration groups. The 6 g/L NaAlO<sub>2</sub> concentration MAO coating demonstrated the highest fitting coating resistance R<sub>3</sub> (8.14 × 10<sup>4</sup> Ω·cm<sup>2</sup>), signifying better corrosion resistance.

**Keywords:** micro-arc oxidation; magnesium alloy; electrolyte; surface modification; corrosion resistance; biomedical material



**Citation:** Zhou, S.-F.; Lu, S.; Lv, W.-G.; Wang, Z.-X.; Oleksandr, D.; Gu, J.-J.; Zhang, J.-W.; Chen, L.-Y. Influence of NaAlO<sub>2</sub> Concentration on the Characteristics of Micro-Arc Oxidation Coating Fabricated on a ZK60 Magnesium Alloy. *Coatings* **2024**, *14*, 353. <https://doi.org/10.3390/coatings14030353>

Academic Editors: Tadeusz Hryniewicz and Stefano Rossi

Received: 29 December 2023

Revised: 12 March 2024

Accepted: 13 March 2024

Published: 16 March 2024



**Copyright:** © 2024 by the authors. Licensee MDPI, Basel, Switzerland. This article is an open access article distributed under the terms and conditions of the Creative Commons Attribution (CC BY) license (<https://creativecommons.org/licenses/by/4.0/>).

## 1. Introduction

Biomedical materials [1–3] are developed to enhance human tissue functions, address medical conditions, or facilitate the repair of injuries. These materials are engineered to meet specific and predefined functions within the physiological environment. Biomedical materials must exhibit exceptional properties to achieve these objectives [4,5]. This result includes the requirement for high mechanical characteristics, encompassing hardness and modulus of elasticity, to withstand the stresses and strains experienced during their service life [6]. Furthermore, these materials must demonstrate remarkable biocompatibility while maintaining minimal or non-toxic attributes [7,8].

Moreover, these materials should exhibit outstanding yet manageable corrosion resistance to mitigate the effects of corrosion induced by the physiological milieu [9–11]. To this end, a promising objective is to enable biomedical materials to incorporate specific therapeutic agents and pharmaceuticals, facilitating controlled and sustained release processes within the physiological context [12,13].

Magnesium alloys, encompassing various series such as Mg-Al, Mg-Zn, and Mg-Ca, have assumed significant roles in biomedical applications [14]. Their increasing adoption,

underpinned by their ability to exhibit mechanical properties akin to human osseous tissue, exceptional biocompatibility, and degradability, has garnered substantial global attention within the research community [15,16].

Using magnesium alloys as implant materials offers the advantage of circumventing the 'stress shielding effect', which can lead to complications like refracture or osteoporosis. It obviates the need for a subsequent removal operation, as is common with stainless steel or titanium implants [17]. Nevertheless, using pure magnesium or specific magnesium alloys with inadequate corrosion resistance can lead to premature degradation before fulfilling their intended service lifespan or the accumulation of alkaline substances and hydrogen within the physiological milieu. Consequently, enhancing their corrosion resistance and other pertinent properties has become imperative in surmounting the challenges above. Surface modification techniques have emerged as a customary approach to mitigate these shortcomings [18–22].

Micro-arc oxidation (MAO), also known as plasma electrolytic oxidation (PEO), constitutes a surface modification technique for alloys [23]. MAO employs electrochemical processes to create in situ porous ceramic coatings on magnesium alloy substrates, endowing them with desirable characteristics such as heightened hardness, enhanced corrosion resistance, and bone-inductive properties.

In the MAO preparation procedure, metallic substrates, such as magnesium, aluminum, and titanium alloys, are immersed in a pre-established electrolyte solution, with a conductive wire linking them to a specialized MAO power supply. Auxiliary equipment, such as an electric transformer and an industrial chiller, are also integrated. The MAO power supply generates a controlled electrical current based on preset parameters, encompassing current mode, voltage, frequency, and duration.

In the preparation of MAO coatings, numerous critical factors exert a substantial impact on their properties. Among these factors, the choice of current mode, electric parameters, and electrolyte plays a pivotal role. Electric parameters, encompassing aspects such as duty cycle, current density, frequency, and duration, have garnered significant attention in recent years. For instance, a study by Chang et al. [24] delved into the influence of voltage, frequency, and duty cycle on MAO coatings. Their findings revealed that an increase in voltage resulted in thicker coatings but a decrease in coating thickness with increasing frequency. Moreover, higher voltage and duty cycle settings adversely affected coating uniformity. Furthermore, the choice of electrolyte used in the preparation process substantially influenced the resulting MAO coating.

Electrolytes employed in the MAO preparation of magnesium alloys encompass a range of compositions, including silicate, aluminate, borate, and tungstate electrolytes [25,26]. Investigation into the influence of these electrolytes has emerged as a prominent research area.

Biomedical MAO coatings, particularly those based on calcium phosphate (Ca-P), often featuring carbonate apatite (C.A.) or hydroxyapatite (H.A.), are renowned for their exceptional biological properties. Introducing  $\text{NaAlO}_2$  into the electrolyte has enhanced the corrosion resistance of MAO coatings [27–31].

In biomedical materials, the assessment of antibacterial activity, which pertains to the capability to suppress or eradicate bacterial growth, assumes substantial importance [32–34]. Efforts have been undertaken to enhance the antibacterial performance of MAO coatings, including strategies involving introducing antibacterial agents or organisms into the coatings [35,36]. Researchers have strongly emphasized augmenting the antibacterial efficacy of MAO coatings, recognizing their critical role in ensuring the success of surgical procedures and postoperative recovery [32,37,38]. Consequently, it becomes imperative to subject MAO coatings to antibacterial testing.

In this study, the optimization of  $\text{NaAlO}_2$  concentration in the electrolyte was carried out by performing univariable experiments. Tests and analyses were also performed to appraise the properties of coating obtained in all groups. This study aimed to optimize the  $\text{NaAlO}_2$  concentration of Al-containing MAO coating, as well as to obtain the best compre-

hensive properties of the coating. The optimized MAO coating can be used to prepared and study on the Al containing MAO/layered double hydroxide composite coating.

## 2. Materials and Methods

### 2.1. Preparation of MAO Coating

Reagents including  $\text{Na}_2\text{SiO}_3 \cdot 9\text{H}_2\text{O}$ ,  $\text{C}_4\text{H}_6\text{CaO}_4 \cdot \text{H}_2\text{O}$ ,  $\text{NaAlO}_2$ ,  $(\text{NaPO}_3)_6$ ,  $\text{NaH}_2\text{PO}_4 \cdot 2\text{H}_2\text{O}$ ,  $\text{NaOH}$ , and  $\text{NaHCO}_3$ , etc., were employed in the MAO coating preparation. All reagents utilized were of analytical purity.

During preparation, the ZK60 magnesium alloy substrates were sectioned into  $15 \text{ mm} \times 15 \text{ mm} \times 5 \text{ mm}$  sheets. Subsequently, these sheets underwent a series of treatments involving grinding with 400#, 800#, and 1000# SiC abrasive paper on a grinding machine, followed by a degreasing process using acetone. The alloy sheets were then immersed in ethanol and distributed into four groups.

According to the previous study of the group, the silicate–phosphate composite electrolyte can be used to obtain MAO coatings with better corrosion resistance and biocompatibility [39]. The precise constituents of these electrolytes are outlined in Table 1. Consequently, the concentrations of  $\text{NaAlO}_2$  in each of the four experimental groups, serving as the independent variable in this study, were set at 3, 6, 9, and 12 g/L, individually.

**Table 1.** Ingredient composition of electrolytes (g/L).

Reagent	$\text{Na}_2\text{SiO}_3$	$(\text{NaPO}_3)_6$	$\text{Ca}(\text{Ac})_2$	$\text{NaH}_2\text{PO}_4$	$\text{NaAlO}_2$	$\text{NaOH}$
Concentration	6.0	0.8	0.5	0.5	3, 6, 9, and 12 g/L	Adjust pH value to 13

In this research, the WHD-30 micro-arc oxidation power supply, sourced from the Harbin Institute of Technology, was employed with a three-phase transformer and an industrial chiller to prepare MAO coatings. It is crucial to note that the three-phase transformer and the industrial chiller must be activated before initiating the MAO power supply. Before the MAO preparation process commenced, meticulous attention was directed toward the configuration and verification of electrical parameters associated with the MAO power supply. These parameters included the selection of current mode, voltage, current magnitude, and duty cycle.

A pre-prepared sheet was secured to a steel wire with a cylindrical piece of ethoxylate resin during each preparatory phase. The electrolyte solution was subsequently introduced into the electrolyzer, and the liquid level needed to submerge the entire sheet while only partially covering half of the cylindrical resin protruding above the sheet's surface. The wire was connected to the anode of the electrolyzer. The specific electrical parameters adopted in this study are detailed in Table 2 and were configured through manual input via the control panel of the MAO power supply.

**Table 2.** Electrical parameters of MAO preparation.

Current Mode	Current Density ( $\text{A}/\text{dm}^2$ )	Frequency (Hz)	Duty Circle (%)	Positive/Negative Pulse Ratio	Duration (s)
Constant current	20	600	30/70	1/1	300

The power supply was activated upon the comprehensive verification of all equipment and parameters to initiate the preparation process. Subsequently, the resulting coating was subjected to an ethanol immersion step for oxidative treatment in preparation for subsequent testing and analytical procedures.

## 2.2. Microstructure and Chemical Analysis

The JSM-6480 SEM by JEOL (Tokyo, Japan), served as the primary instrument for examining the impact of  $\text{NaAlO}_2$  concentration on the microstructure of the MAO coating, encompassing both superficial and cross-sectional morphological characteristics. Complementary analytical techniques included energy-dispersive X-ray spectroscopy (EDS) to ascertain the elemental composition and distribution within the MAO coating.

A range of sophisticated instrumentation was employed to facilitate these comprehensive investigations. The XRD-6000 X-ray diffraction (XRD) system from Shimadzu (Tokyo, Japan) experimental parameters including the scanning speed was  $4^\circ/\text{min}$ , scanning range was from  $20^\circ$  to  $80^\circ$ , and voltage was 40 kV; XPS was utilized to assess the chemical composition, phase composition, and chemical bonds present in the coating. Additionally, the Olympus LEXTOLS4000 Confocal Laser Microscope (Tokyo, Japan) was employed to quantify the linear surface roughness of the coating and generate three-dimensional surface morphology profiles.

## 2.3. Mechanical Properties

The assessment of mechanical properties is essential for ensuring the integrity of coatings throughout their intended service life. In this study, particular attention was given to the impact of  $\text{NaAlO}_2$  concentration on the hardness and adhesive properties of MAO coatings, necessitating a systematic examination of these mechanical attributes.

Adhesive properties, reflecting the interaction between the MAO coating and the underlying Mg alloy substrate, were evaluated through nano scratch tests and circumferential abrasion tests. The CSM-NHT2 Nanoindentation Tester, manufactured by CSM Instruments (Montreal, QC, Canada), was employed for conducting these assessments. The maximal load was 15 N, and the test course was 3 cm. Concurrently, hardness, signifying the resistance of the MAO coating to applied pressure, was a pivotal characteristic under investigation. This study involved measuring and comparing the coating's hardness to discern the effects of varying  $\text{NaAlO}_2$  concentrations. The hardness test was performed by selecting 5 measuring points arranged in a regular pentagon, as illustrated in Figure 1. The average hardness value across these 5 points was considered the evaluating indicator within each group.

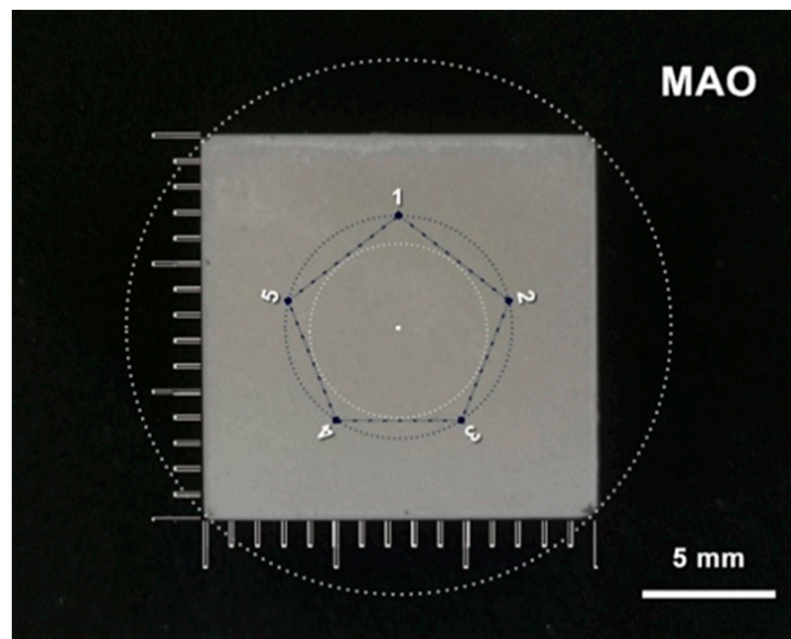


**Figure 1.** Measuring position for the microhardness of the MAO specimen surface.

#### 2.4. Antibacterial Test

The antibacterial assessment was conducted to evaluate the capacity of coatings within the human body environments to inhibit and deter bacterial cell division and propagation. In clinical medical applications, bacterial infections and inflammation are the primary factors contributing to implant failure.

The antibacterial tests were conducted within biological laboratories, utilizing specialized equipment and instruments, including an autoclave, a thermostatic water bath oscillator, a vertical clean bench, an ultraviolet spectrophotometer, a biochemical incubator, a centrifuge, and various glass containers. Additionally, consumables such as *Escherichia coli* (*E. coli*), beef extract peptone medium (BPM), beef extract peptone agar medium, and normal saline were employed.

All glass vessels, containers, and centrifuge tubes were meticulously wrapped in newspaper and securely sealed with rubber bands to prepare for the experiment. Subsequently, they underwent sterilization in an autoclave at 120 °C for a minimum of 40 min.

The experiment commenced with the activation of *E. coli*, which had been refrigerated at 0 °C. This activation involved placing the *E. coli* into pre-prepared BPM and cultivating it in a thermostatic shaker incubator at 37 °C for 24 h. The resulting liquid culture of *E. coli* was divided into five equal portions. Four portions contained samples of MAO coating prepared with NaAlO<sub>2</sub> electrolyte concentrations of 3, 6, 9, and 12 g/L, individually, while the fifth served as the control group.

All portions were stored in a thermostatic incubator for 18–24 h of cultivation. Following the incubation, each portion of the *E. coli* liquid underwent an absorbance test in an ultraviolet spectrophotometer to ascertain and adjust the bacterial concentration as needed for subsequent experiments. A dilution process was then performed, involving the extraction of 1 mL of *E. coli* liquid into two centrifuge tubes, followed by centrifugation at 2000 r/min for 2 min. Afterward, 0.5 mL of the condensed *E. coli* at the bottom of both tubes was extracted, and this was combined to form 1 mL of primary *E. coli*. This primary *E. coli* liquid was diluted to 10<sup>-7</sup> of the original concentration by repeating the extraction–centrifuge–dilution steps.

Subsequently, for each group, the diluted liquid was thoroughly agitated using a shaker, and 200 µL of the diluted *E. coli* liquid was carefully applied to a solid medium plate using a right-angle glass rod. After 20 min of drying in ambient conditions, the coated solid medium plates were stored in a thermostatic incubator at 37 °C for 24 h. The antibacterial activity of the MAO coating was determined by counting the bacterial colonies on each solid medium plate, with a smaller number of colonies indicating a stronger antibacterial effect.

#### 2.5. Water Contact Angle Test

In assessing the biocompatibility of implants within in vivo or in vitro environments, a fundamental criterion is the measurement of the water contact angle, which reflects the implant's capability to perform its designated functions without inducing pathological disorders or inflammation. A JC2000D1 contact angle meter (Shaanxi, China) was employed, employing a static method to quantify the angle between the edge of a water droplet and the surface of the coating, referred to as the water contact angle. Multiple measurements of each coating were undertaken to derive an average value. For each test, a water droplet of 0.4 µL was used under the ambient temperature of 20 °C.

#### 2.6. Corrosion Resistance Test

The durability of MAO coating on Mg alloy substrates within the human body fluid environment is crucial, as it directly impacts the implant's ability to fulfill its intended service life. Therefore, it is imperative to employ methodologies for the comprehensive examination, analysis, and evaluation of the corrosion resistance of MAO coatings.

The corrosion resistance assessment of MAO coatings encompasses various approaches. In the specific context of this study, the Mg substrate was coated using a NaAlO<sub>2</sub>-silicate-

phosphate electrolyte. In the human body environment, the equilibrium electrode potential for Mg is  $-2.375 \pm 0.005$  V [40].

The corrosion rate is a pivotal evaluation criterion to gauge and compare the corrosion resistance of MAO coatings. It can be determined through methods such as the weight loss technique or the hydrogen evolution test. This investigation employed the weight loss method to compute the corrosion rate. Preparatory steps included cutting the Mg alloy substrate into  $15 \text{ mm} \times 15 \text{ mm} \times 5 \text{ mm}$  specimens before coating application. These samples underwent meticulous degreasing and cleaning. Ensuring their suspension in the solution is essential to prevent sinking. The calculation of corrosion rate, presented as Formula (1), was performed to compare the corrosion resistance of MAO coating,

$$V = \frac{W_0 - W_1}{AT} \quad (1)$$

The average corrosion rate ( $V$ ) of the sample, expressed in  $\text{mg}/(\text{mm}^2 \cdot \text{day})$ , was calculated by measuring the difference between the initial mass of the sample ( $W_0$  in mg) and its mass after immersion ( $W_1$  in mg); the difference of mass was then divided by the sample's surface area ( $A$ ) multiplying the duration of immersion ( $T$ ). The immersion tests involved placing the samples in Hank's solution, the composition of which is detailed in Table 3. This Hank's solution needed to be meticulously prepared using deionized water, and its pH value needed to be adjusted to 7.5 with  $\text{NaHCO}_3$ , followed by the adjustment of the solution volume to 2 L, and, lastly, sterilization. The samples were tied with cotton thread with different colors to distinguish their groups. They were placed in the Hank's solution, with the ratio of solution volume to sample superficial area kept at 10. The samples were soaked in the solution for 5, 10, 15, and 20 days, and the Hank's solution was replaced every 24 h.

**Table 3.** Ingredients of Hank's solution (mM).

$\text{CaCl}_2$	KCl	$\text{KH}_2\text{PO}_4$	$\text{MgSO}_4$	NaCl	Glucose	$\text{Na}_2\text{HPO}_4$	Phenol Sulfonphthalein
1.3	5.4	0.4	0.8	137	5.6	0.34	0.03

The CHI6600E electrochemical workstation, Chenhua Instruments (Shanghai, China) together with the associated CH Instruments Electrochemical Software version 1.03, were employed to assess the electrochemical impedance of MAO coating. MAO samples previously fabricated were connected to conductive Al wires, together they were covered by the insulating silicone, the joint of samples and the connecting wires must be assured to be covered perfectly. While a  $10 \times 10 \text{ mm}$  square was drawn on the proper  $15 \times 15 \text{ mm}$  surface was defined as the testing area. The whole samples should be covered by the insulating silicone except for the designated testing area. The treated samples were dried in the ambient air for at least 24 h. The experiment process began with the measurement of open circuit potential over 1800 s. The value obtained from OCPT served as the potential value, with a high frequency of 100,000 V, a low frequency of 0.01 Hz, an amplitude of 0.01 V, and a quiet time of 2 s. All these parameters were applied in the impedance test, and the two tests were put into practice under the ambient temperature of 20 degrees Celsius. The test results were firstly fitted with a software named Zsimpwin v3.60 to obtain the approximate range of the fitting results, and then the original data were placed in the software named ZView2 v3.0.0.22 to perform an accurate fitting process. The fitted results were drawn into the Nyquist and Bode diagrams.

The ingredients and medicines being used in this paper with their manufacturers are presented in Table 4.

**Table 4.** Ingredients and chemicals used.

Medicines	Manufacturer	Purity
Na <sub>2</sub> SiO <sub>3</sub>	Macklin, Shanghai, China	Analytic pure (AR)
(NaPO <sub>3</sub> ) <sub>6</sub>	Macklin, Shanghai, China	AR
Ca(Ac) <sub>2</sub>	Macklin, Shanghai, China	AR
NaH <sub>2</sub> PO <sub>4</sub>	Macklin, Shanghai, China	AR
NaAlO <sub>2</sub>	Macklin, Shanghai, China	AR
NaOH	Macklin, Shanghai, China	AR
Hank's solution	Beijing Solarbio Science and Technology Co., Ltd., Beijing, China	AR

### 3. Results and Analyses

#### 3.1. Influence of NaAlO<sub>2</sub> Concentration on MAO Electrochemical Phenomena

Within the MAO preparation process, the NaAlO<sub>2</sub> concentration directly and perceptibly impacted the electrolyte and the overall reaction dynamics. Electrical conductance and reaction voltage were employed to assess the changes in the electrolyte, while macroscopic reaction observations revealed the NaAlO<sub>2</sub> concentration's effects on the reaction phenomena to investigate this influence.

##### 3.1.1. Influence on Electrical Conductance

As previously mentioned, NaAlO<sub>2</sub> concentrations were systematically varied among the four groups, specifically at 3 g/L, 6 g/L, 9 g/L, and 12 g/L. To investigate their impact on the electrolyte, electrical conductance, a parameter characterizing a material's ability to convey and facilitate electric current, was quantified across all groups, with the results presented in Figure 2.

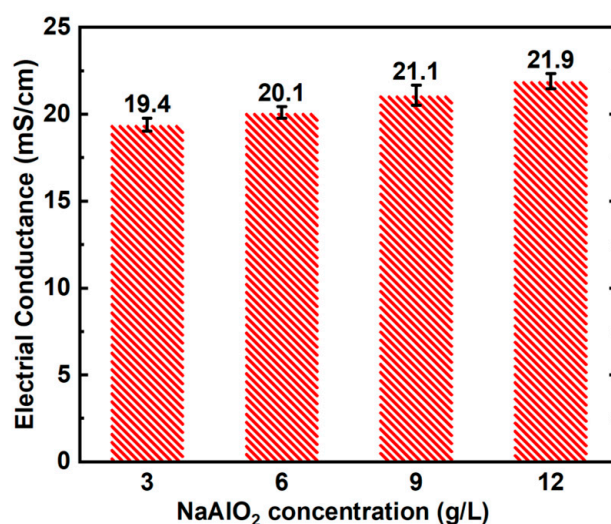
**Figure 2.** Influence of NaAlO<sub>2</sub> concentration on electrolyte conductance.

Figure 2 shows that the electrical conductance of the silicate–phosphate composite electrolyte exhibited a positive correlation with the concentration of NaAlO<sub>2</sub>. The conductance increased from 19.4 to 20.1 mS/cm as the NaAlO<sub>2</sub> concentration escalated from 3 to 6 g/L. However, subsequent increments in NaAlO<sub>2</sub> concentration yielded a proportionally weaker rise in electrical conductance. Considering the well-established connection between electrical conductance and the ionic content within the electrolyte [41], it was postulated that the marked augmentation of AlO<sub>2</sub><sup>−</sup> ions resulted in the observed augment of electric conductance. It is essential to underscore that NaAlO<sub>2</sub> qualifies as a potent electrolyte, displaying complete dissolution and dissociation in aqueous solutions, thus it becomes an efficient conductor of electrons and electric currents [42].

### 3.1.2. Influence on Reaction Voltage

This section focuses on the meticulous measurement of arcing and cut-off voltage to delve into the intricacies of MAO preparation. These crucial voltage parameters were meticulously recorded using the functionalities embedded in the manual panel of the MAO power supply. Arcing voltage, a pivotal metric, denotes the voltage threshold at which the initial formation of an electric arc becomes perceptible on the substrate's surface. In contrast, the cut-off voltage signifies the pinnacle voltage attained in the later phases of the MAO process, unfolding between the cathode and anode.

Throughout this investigation, the constant current mode remained consistently employed in the concluding stages of the MAO coating preparation. In adhering to Ohm's law, encapsulated as Formula (2), the voltage indicated the electric resistance within the electrolyzer, owing to the steadfast current (I). Consequently, the voltage positively correlated with the resistance (R), a relationship that translated into the thickness of the resulting MAO coating.

$$I = \frac{U}{R} \quad (2)$$

Figure 3 illustrates the impact of  $\text{NaAlO}_2$  concentration on the reaction voltage. In the  $\text{NaAlO}_2$  group, the arcing voltage was registered at 247 V. In contrast, the cut-off voltage was measured at 458 V. Introducing  $\text{NaAlO}_2$  into the electrolyte solution led to a decrease in arcing voltage and an increase in cut-off voltage. Specifically, in the 6 g/L group, the arcing voltage diminished by 33 V, and the cut-off voltage rose by 12 V. In the 12 g/L group, the arcing voltage experienced a significant reduction to 188 V, whereas the cut-off voltage increased to 489 V.

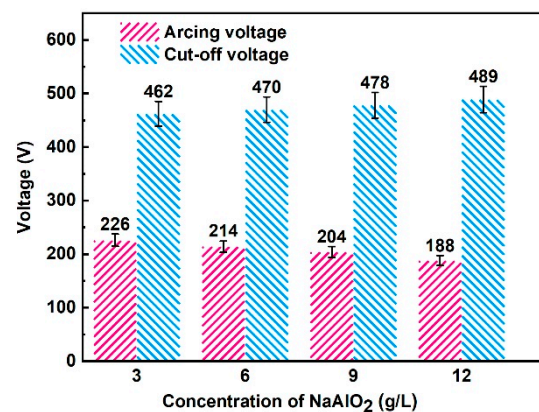


Figure 3. Influence of the  $\text{NaAlO}_2$  concentration on reaction voltage.

The decline in arcing voltage can be attributed to the greater presence of reactive ions, which facilitate the electrochemical reactions within the MAO process. Conversely, the cut-off voltage was linked to phenomena such as arc breakdown, point discharge, and coating ablation, which can potentially compromise the surface quality of the MAO coating. The variation in voltage values can be chiefly ascribed to the  $\text{NaAlO}_2$  concentration, as  $\text{NaAlO}_2$  released  $\text{Al}^{3+}$  ions into the electrolyte, enhancing their corrosion resistance and surface uniformity.

Table 5 presents the observed reaction phenomena during MAO preparation in each respective group. The addition of  $\text{NaAlO}_2$  into the electrolyte had two notable consequences. Firstly, it intensified the later stages of the MAO reaction, leading to nonuniformity on the coating surface due to partial, continuous discharges within the coating while other sections remained unaffected. Secondly, adding  $\text{NaAlO}_2$  introduced instability into the system, evidenced by the formation of flocculation, specifically  $\text{Al}(\text{OH})_2$ , during the MAO process. In the 12 g/L group, notable features included the presence of significant quantities of white suspension; vigorous point discharges; and, in extreme cases, ablation.

**Table 5.** Reaction phenomena of different groups of coatings.

Concentration of NaAlO <sub>2</sub> (g/L)	Reaction Phenomena
3	Bubbles around the anode arc unstable in a later period, with a discontinuous beeping sound.
6	Bubbles were floating, white foam on the liquid surface, and a continuous beeping sound until the reaction ended.
9	Bubbles floating; obvious elevation of electrolyte temperature; suspension appeared; loud beeping sound.
12	Fierce bubble floating; electrolyte seethed at 4 min; quantities of suspension in liquid; harsh beeping sound.

A clear positive correlation was evident between NaAlO<sub>2</sub> concentration and cut-off voltage, while an inverse relationship existed between NaAlO<sub>2</sub> concentration and arcing voltage. This phenomenon can be primarily attributed to NaAlO<sub>2</sub> concentration variations, aligning with previous research findings [43]. These findings underscore the impact of single-ingredient concentration on voltage values; coating thickness; and, consequently, coating corrosion resistance [44].

### 3.2. Influence of NaAlO<sub>2</sub> Concentration on the Morphology of MAO Coating

#### 3.2.1. Superficial Morphology Analysis

In this section, the influence of NaAlO<sub>2</sub> concentration on the superficial morphology of the MAO coating is studied through SEM tests. Figure 4 reveals distinctive structures such as micropores, cracks, and melts. Melts were predominantly concentrated around micropores, collectively shaping a distinctive ‘volcanic structure’. An intriguing phenomenon was observed, shown within the dotted white circle in Figure 4b,c, where smaller micropores existed within larger pores.

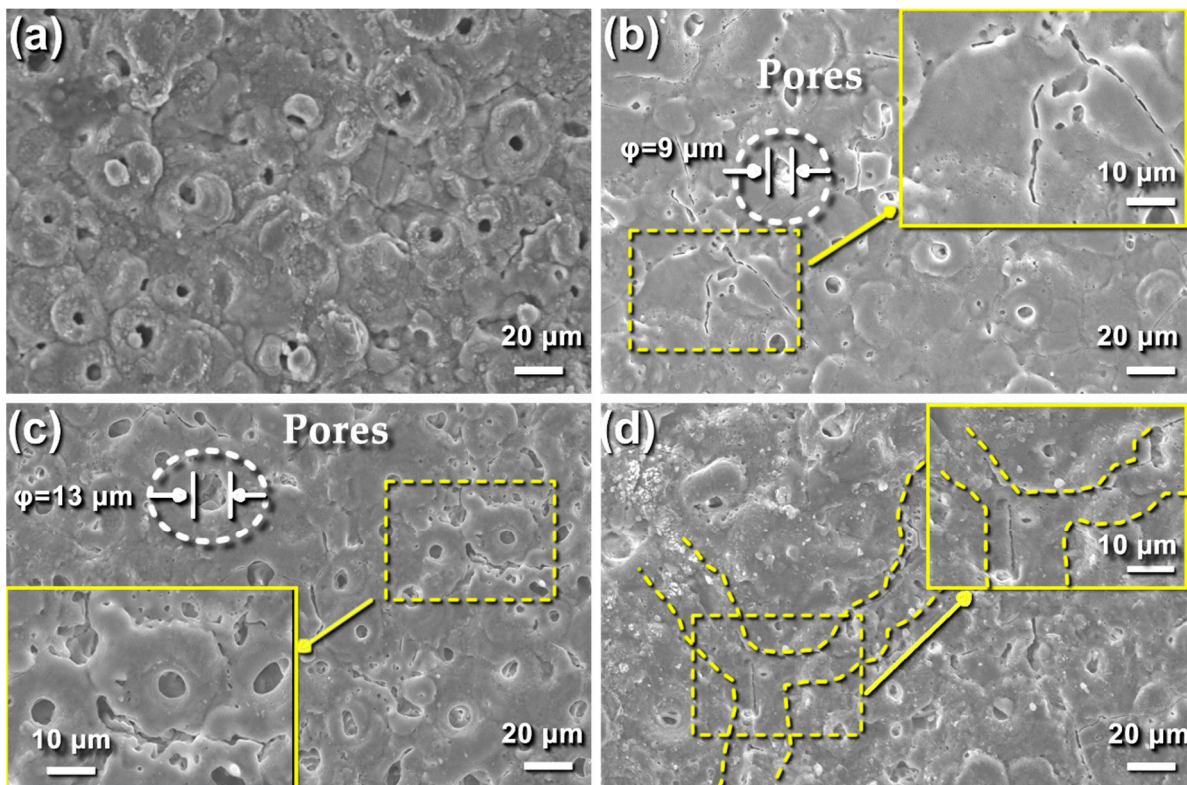


**Figure 4.** SEM image of the MAO coatings prepared with different NaAlO<sub>2</sub> concentrations: (a) 3 g/L; (b) 6 g/L; (c) 9 g/L; (d) 12 g/L.

The formation of melts resulted from the intricate process involved in MAO coating preparation, wherein the discharge channel underwent electric breakdown, leading to the repeated accumulation and reformation of melts before finishing [45]. For a comprehensive overview, Table 6 presents the influence of NaAlO<sub>2</sub> concentration on the porosity of the MAO coating. The porosity of the coating was calculated by using the software ImageJ v1.02, which performs the calculation by using a microscopic SEM image of the coating.

**Table 6.** Porosity of the MAO coatings (%).

NaAlO <sub>2</sub> Concentration (g/L)	3	6	9	12
Porosity	10.5	9.1	12.4	15.5

It can be seen that the porosity exhibited an initial decrease followed by a subsequent increase, with the 6 g/L NaAlO<sub>2</sub> concentration yielding the lowest porosity at 9.1%, distinguishing itself from other concentrations. A discernible negative correlation existed between porosity and the corrosion resistance of the MAO coating [46], with the number of cracks exhibiting an upward trend alongside the NaAlO<sub>2</sub> concentration. Specifically, cracks, predominantly discontinuous and fewer than pores (Figure 4a), became more pronounced in the 12 g/L groups, where continuous cracks spread and certain fissures were prominently formed (Figure 4d).

The emergence of cracks was attributed to the shock-chilling effect of the electrolyte [47]. In the latter stages of the MAO preparation, certain coating regions underwent multiple electrical breakdowns due to significant volume spark discharge phenomena caused by high voltage. Consequently, the electrolyte temperature surged rapidly around these regions, leading to nonuniform growth of the MAO coating and the formation of cracks. These structural defects contributed to an increase in linear roughness, diminished coating compactness, and compromised coating corrosion resistance.

Pores and cracks, conduits for external media to penetrate the intermediate layer of the coating or even reach the substrate, pose a significant threat to the corrosion resistance of the MAO coating. Addressing these issues through defect reduction in the MAO coating or implementing a sealing post-treatment can effectively enhance corrosion resistance [48].

### 3.2.2. Cross-Section Morphology Analysis

The maximum thickness of the MAO coating, highlighted by yellow arrows in Figure 5, was complemented by a presentation of its cross-sectional morphology. There was a consistent escalation in MAO coating thickness with increasing NaAlO<sub>2</sub> concentration in the electrolytes. As depicted in Figure 5a,c, the MAO coating thickness ranged from 32.2 μm to 70.9 μm, correlating with an augmentation of the NaAlO<sub>2</sub> concentration from 3 g/L to 12 g/L. An observation revealed a higher prevalence of pores and cracks in MAO coatings with augmented thicknesses.

In the 6 g/L and 9 g/L groups, the MAO coating attained an optimal thickness, exhibiting an acceptable pore count, with the absence of any continuous cracks traversing the entire MAO coating from the substrate to the external surface. However, in the 12 g/L groups, despite the heightened coating thickness, the nonuniformity and undulating morphology induced by large-volume spark discharge and growth rate disparities among regions contributed to the development of penetration cracks and fissure belts. These structural features acted as conduits, facilitating the flow of external fluid to the junction of the substrate and coating, resulting in diminished corrosion resistance. To emphasize this, Figure 5d illustrates how multiple cracks and pores collectively formed the coating, marked by a white dotted circle.

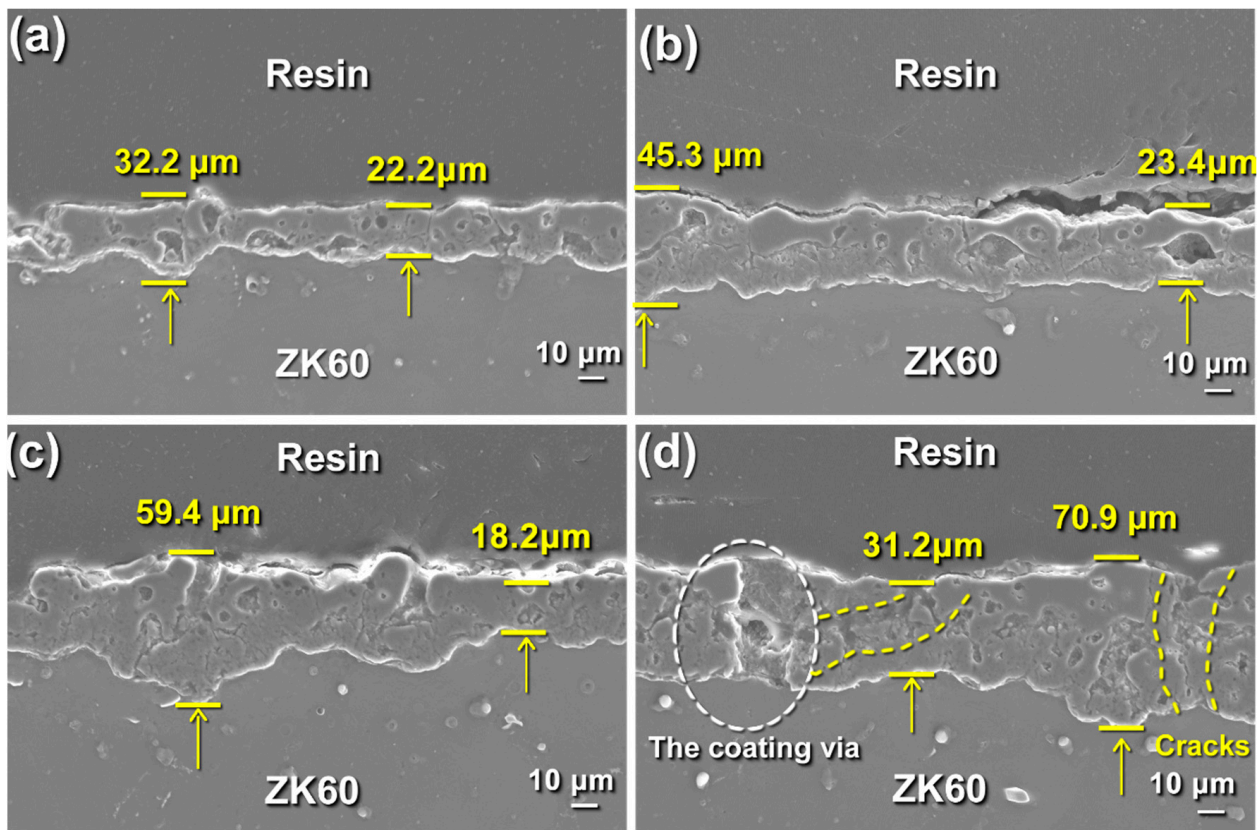


**Figure 5.** Cross-section SEM image of the MAO coatings prepared with different  $\text{NaAlO}_2$  concentrations: (a) 3 g/L; (b) 6 g/L; (c) 9 g/L; (d) 12 g/L.

### 3.2.3. Linear Roughness Analysis

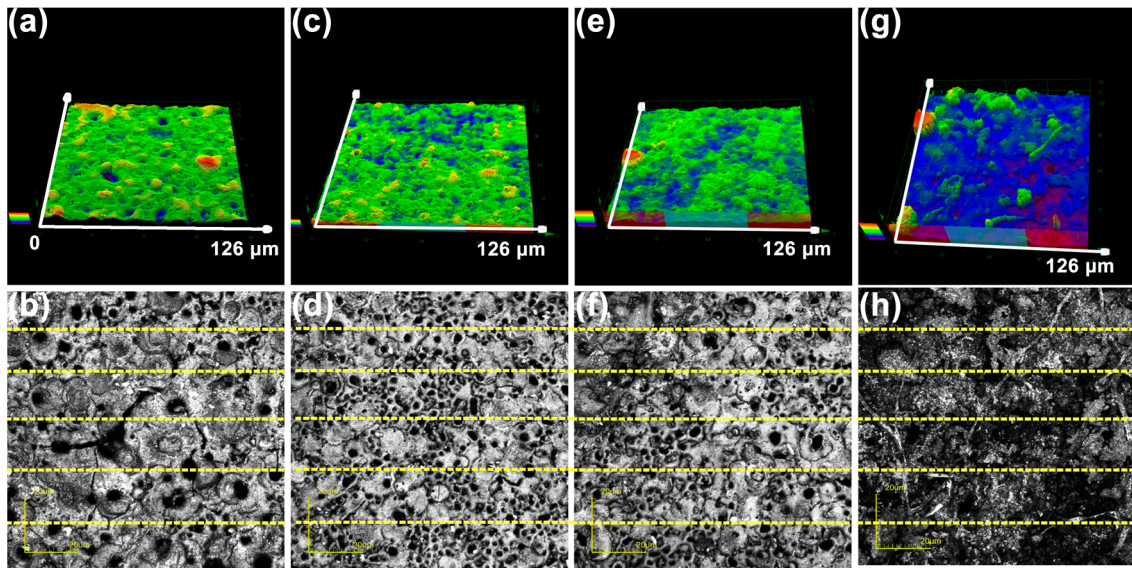
Linear roughness is an important indicator of the coating’s flatness and uniformity [49]. This metric was quantified and extracted using the confocal laser microscope, which provides both two-dimensional and three-dimensional morphological graphs.

Figure 6 showcases both two-dimensional and three-dimensional morphological graphs, providing a visual representation of the coating that facilitates the global observation of mesoscopic defects and cracks. In the three-dimensional graphs, colors denote variations in altitude on the coating surface, where blue regions signify lower and hollow parts while yellow and red represent highland and volcanic peaks. Although these visuals offer intuitive insights, they are unreliable for quantitative analysis. Therefore, the linear roughness can serve as a statistical measure and facilitating accurate calculations.

The linear roughness data for four MAO coating groups are detailed in Table 7. Five measurements were conducted on a single sample within each group to yield five linear arithmetic average roughness values ( $R_a$ ) at different positions, as illustrated in Figure 6b,d,f,h, with the measured positions indicated by dotted yellow lines. These  $R_a$  values are then represented in the linear roughness distribution chart (Figure 7).

**Table 7.** Linear roughness of the MAO coatings with various  $\text{NaAlO}_2$  concentrations ( $\mu\text{m}$ ).

NaAlO <sub>2</sub> Concentration (g/L)	Data 1	Data 2	Data 3	Data 4	Data 5
3	3.016	3.016	2.792	3.089	2.792
6	2.709	2.537	2.576	2.442	2.700
9	3.072	3.140	2.797	3.118	3.591
12	3.121	3.452	3.266	3.591	3.485



**Figure 6.** Two-dimensional morphology: (a) 3 g/L; (c) 6 g/L; (e) 9 g/L; (g) 12 g/L. Three-dimensional morphology: (b) 3 g/L; (d) 6 g/L; (f) 9 g/L; (h) 12 g/L.

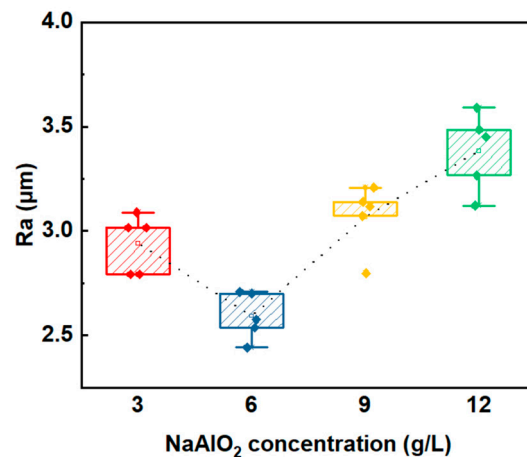


**Figure 7.** Distribution chart of the linear roughness of the MAO coatings prepared with different NaAlO<sub>2</sub> concentrations.

Analysis of the chart revealed a significant fact: an initial decline took place in linear roughness, followed by a subsequent increase with an escalating NaAlO<sub>2</sub> concentration in the electrolyte. Specifically, the 3 g/L group exhibited an average linear roughness of approximately 2.941 μm. The 6 g/L group featured a lower value of 2.5928 μm. The further addition of NaAlO<sub>2</sub> into the electrolyte resulted in an upward trajectory of the roughness Ra, with average values of 3.067 μm for the 9 g/L group and 3.383 μm for the 12 g/L group.

The preceding investigation revealed a significant distinction in Ra values, with the 6 g/L group exhibiting substantially lower values than other groups. This finding directly implies that the flatness and uniformity of the MAO coating in the 6 g/L group surpassed those in the remaining groups.

Taking superficial morphology, cross-section morphology, and linear roughness together into consideration, a consistent relationship emerged between NaAlO<sub>2</sub> concentrations and the resultant morphologies and roughness. Specifically, as NaAlO<sub>2</sub> concentration increased, there was a coherent trend in morphological features and roughness. Initially, with the introduction of more NaAlO<sub>2</sub>, defects such as pores and cracks experienced a decline, adversely affecting the uniformity of the MAO coating.

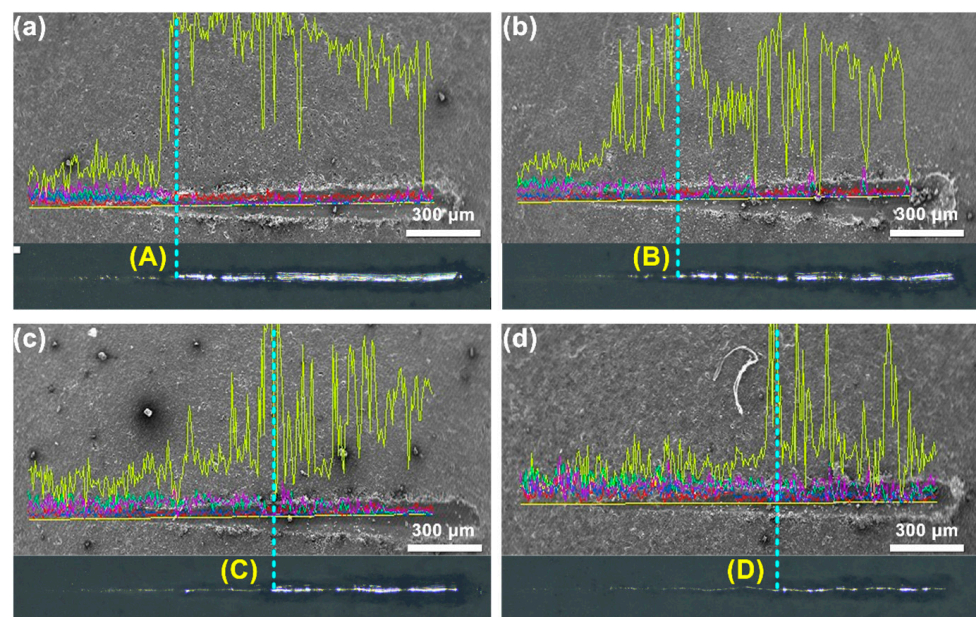
### 3.3. Influence of $\text{NaAlO}_2$ Concentration on the Mechanical Properties of MAO Coating

The mechanical properties, such as hardness, and adhesive force, are important in the performance and durability of MAO coatings throughout their service life. Coatings characterized by inferior mechanical properties can have detrimental effects [50,51]. Consequently, it is imperative to undertake a comprehensive study and analysis to discern the influence of  $\text{NaAlO}_2$  concentration on the mechanical properties of MAO coatings.

#### 3.3.1. Nano Scratch Test

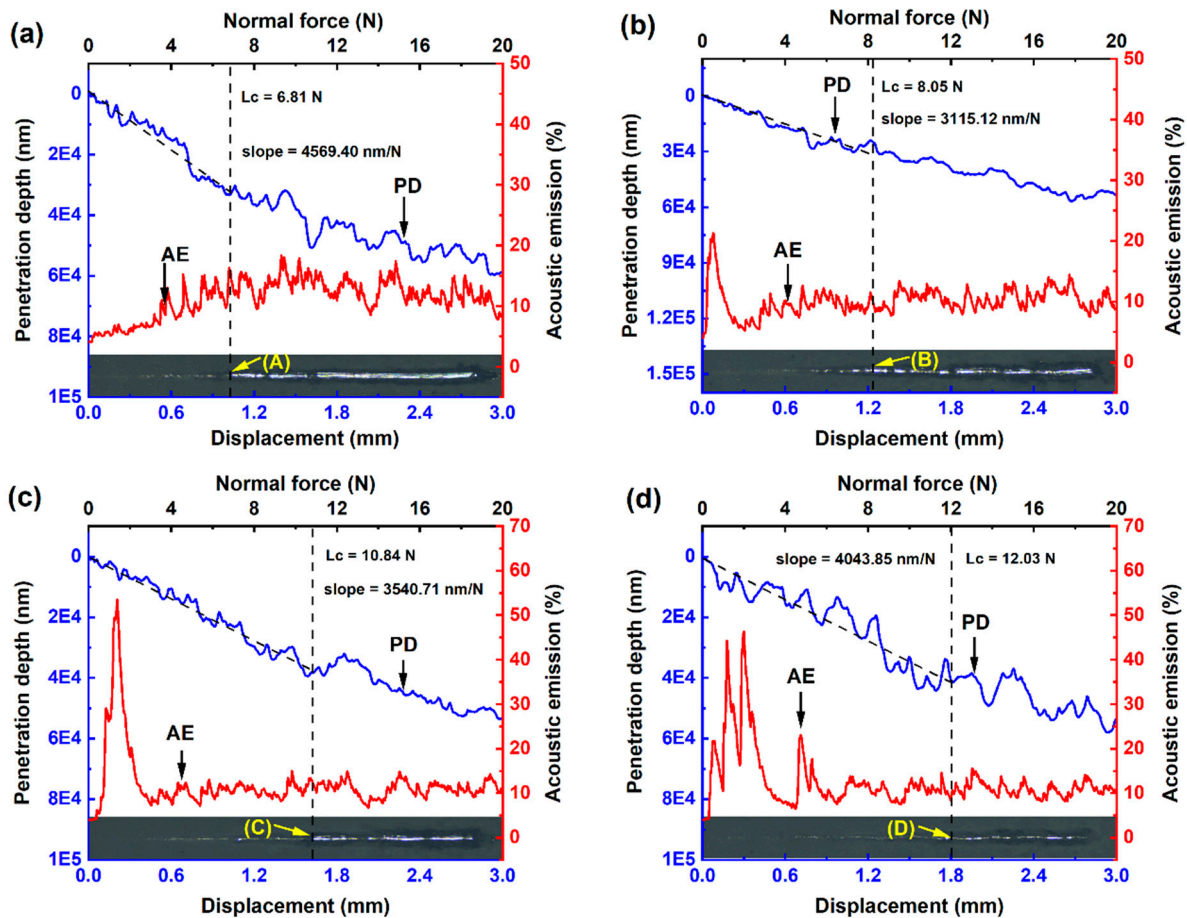
This section assesses the adhesive force of MAO coatings prepared with varying  $\text{NaAlO}_2$  concentrations using nano scratch tests. In the test, the elemental composition and distribution of the coating were also investigated through EDS linear scanning, which aided in defining the puncture point of the MAO coating under testing. Specifically speaking, the position where Mg content underwent a sudden and significant increase in elemental distribution was considered the puncture point in this study. The nano scratch test involves a preload of 20 N, with the load moving 3 mm on the MAO coating surface at a speed of  $3 \text{ N}\cdot\text{mm}^{-1}$ .

Figure 8 presents the results of the EDS linear scanning. As previously described, the puncture point for each coating is denoted by blue vertical dotted lines, accompanied by yellow markings of (A), (B), (C), and (D).



**Figure 8.** EDS linear scanning results of the nano scratch test (the yellow line indicates the change of Mg element content): (a) 3 g/L; (b) 6 g/L; (c) 9 g/L; (d) 12 g/L.

Figure 9 illustrates the results of four groups of nano scratch tests conducted on MAO coatings. In the context of the graphs,  $L_c$  represents the load at which the indenter punctured the MAO coating. The scratch profile was placed below the acoustic emission (A.E.) curve, while the penetration depth (P.D.) curve represents the penetration situation, of which the gradient until puncture points reflects the difficulty of the indenter in penetrating the MAO coating. A lower gradient indicated increased difficulty. Due to the presence of severe nonuniformity and brittle phases in the MAO coating, the A.E. signal exhibited significant fluctuations.



**Figure 9.** Nano scratch testing results of the MAO coatings prepared with different concentrations of NaAlO<sub>2</sub>: (a) 3 g/L; (b) 6 g/L; (c) 9 g/L; (d) 12 g/L.

Observing the Lc values that stand for the load values at the puncture points shown in Figure 9, it was evident that Lc increased from 6.81 N in the 3 g/L group to 12 N in the 12 g/L group, suggesting an escalation in the difficulty of puncturing the MAO coating. This finding implies an augmentation in the adhesive force between the Mg substrate and the MAO coating. However, considering the presence of brittle phases in the coating, which can also contribute to increased puncture difficulty, a detailed analysis of the penetration depth curve is necessary. The gradient of the P.D. curve in the 3 g/L group before puncture was 4569.40 nm·N<sup>-1</sup>, while the gradients in the 6 g/L, 9 g/L, and 12 g/L groups were 3115.12 nm·N<sup>-1</sup>, 3540.71 nm·N<sup>-1</sup>, and 4043.85 nm·N<sup>-1</sup>, respectively. The 3 g/L group exhibited the highest gradient, indicating that its coating was the easiest for the indenter to puncture, likely due to its lower thickness.

Considering the A.E. curve, the MAO coating in the 6 g/L group displayed the most stable acoustic emission. Despite having a lower coating thickness than the 9 g/L and 12 g/L groups, it appeared to have fewer brittle phases or defects. Upon reaching 0.2 mm, the A.E. curve revealed enormous peaks in the 9 g/L and 12 g/L groups, suggesting significant damage and a substantial increase in nonuniformity. Researchers have found that certain coating phases produced during preparation can enhance wear resistance. For instance, hydroxyapatite (H.A.) enhances the wear resistance of MAO coating, and graphene influences the wear and corrosion resistance on a titanium substrate [52,53].

### 3.3.2. Circumferential Abrasion Test

Figure 10 presents the results of the circumferential test conducted on MAO coatings prepared with different NaAlO<sub>2</sub> concentration in the electrolytes. The indicator of the test was the abrasion area. The circumferential abrasion test applied a load of 10 N, a

test duration of 600 s, and a 3 mm abrasive radius for the steel sphere indenter. The five measuring positions for each abrasion arc are represented in Figure 10A0, and the measurement was realized by using a confocal laser microscope, with the average value calculated within each group before further analyses. Table 8 provides the wearing area results calculated from the circumferential tests.

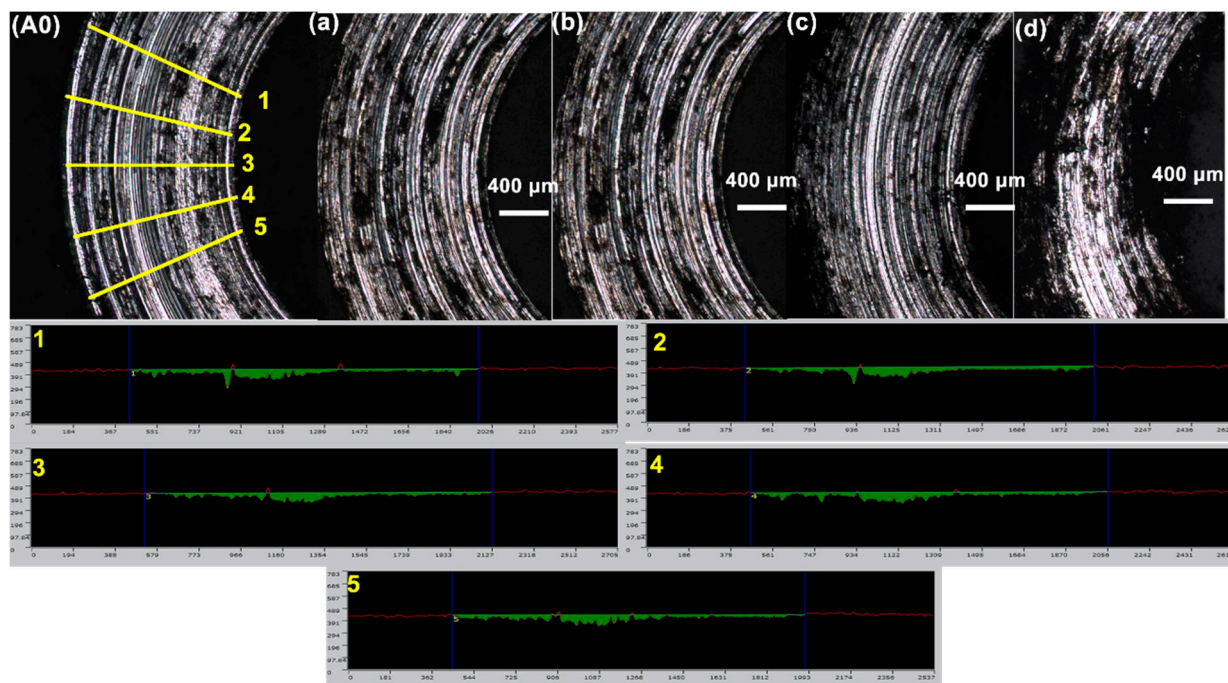


**Figure 10.** Circumferential abrasion morphology of the MAO coating prepared with different  $\text{NaAlO}_2$  concentrations: (A0) display of 5 measuring lines for each sample (a) 3 g/L; (b) 6 g/L; (c) 9 g/L; (d) 12 g/L.

**Table 8.** Wearing area of the MAO coatings prepared with different  $\text{NaAlO}_2$  concentrations ( $\mu\text{m}^2$ ).

NaAlO <sub>2</sub> Concentration (g/L)	Wearing Area $\times 10^{-4}$					Average Value
	1	2	3	4	5	
3	6.38	6.57	6.21	6.57	6.59	6.46
6	2.78	2.49	2.72	3.08	3.49	2.91
9	3.49	3.44	3.53	3.58	3.23	3.46
12	3.98	3.99	3.72	3.83	3.77	3.86

Observations revealed a substantial decrease in the wearing area with increased  $\text{NaAlO}_2$  concentrations. In the 3 g/L group, the average abrasive area was  $6.46 \times 10^4 \mu\text{m}^2$ , while in the 12 g/L group, the average abrasive area decreased to  $2.91 \times 10^4 \mu\text{m}^2$ . A negative correlation existed between the wear area and the wear resistance of the coating. A smaller wear area indicated enhanced wear resistance.

### 3.3.3. Hardness

In this section, the automatic microhardness tester was utilized to measure the microhardness of the MAO coatings.

Table 9 shows an increase in the microhardness of the MAO coating with the rise in  $\text{NaAlO}_2$  concentration. Considering the concurrent prevalence of reaction phenomena, it can be inferred that an elevated presence of  $\text{NaAlO}_2$  in the electrolyte prompted heightened reactivity. Consequently, the formation of high-temperature brittle phases, such as  $\text{MgAl}_2\text{O}_4$ , and the proliferation of defects, such as cracks, were significantly amplified. This escalation results in the generation of micro fragments during the abrasion test. A portion

of these fragments contributes to an increased frictional force between the indenter and the coating.

**Table 9.** The hardness of MAO coatings prepared with different NaAlO<sub>2</sub> concentrations (HV).

NaAlO <sub>2</sub> Concentration (g/L)	Average Value	Standard Deviation
3	349.4	4.3
6	411.2	2.8
9	385.8	2.8
12	374.8	3.8

Considering previous testing results, the coating prepared with 12 g/L encountered large volume spark discharge and nonuniform growth, leading to an uneven distribution of defects in the MAO coating. Consequently, during the abrasion test, this nonuniform distribution caused certain parts to break earlier than others, producing fragments that further damaged the coating surface.

3.4. Influence of NaAlO<sub>2</sub> on Phase and Chemical Bonds

Figure 11 illustrates the XRD patterns both prior to and following the introduction of NaAlO<sub>2</sub> into the electrolyte. In the absence of NaAlO<sub>2</sub>, the XRD pattern revealed the prevalence of MgO and Mg<sub>2</sub>SO<sub>4</sub> as the primary phases in the MAO coating, with Mg<sub>2</sub>SiO<sub>4</sub> representing the high-temperature phase found in the Earth’s mantle at depths ranging from 350 to 1000 km [54]. Contrastingly, the XRD pattern with NaAlO<sub>2</sub> exhibited MgAl<sub>2</sub>O<sub>4</sub> and MgO as the dominant phases, accompanied by a global weakening of MgO diffraction peaks. This weakening suggests a reduction in MgO within the MAO coating and the near disappearance of the secondary peak at 52° for MgSiO<sub>4</sub>. In the NaAlO<sub>2</sub>-included pattern, the MgAl<sub>2</sub>O<sub>4</sub> diffraction peak significantly surpassed that of MgO. Considering the MAO reactions, it was evident that the NaAlO<sub>2</sub>-included electrolyte reacted with the Mg alloy substrate, yielding the high-temperature phase MgAl<sub>2</sub>O<sub>4</sub>, known for its impressive properties, including a high melting point of 2135 °C [55]. It has outstanding high-temperature mechanical properties and chemical stability. Its Knoop hardness is 1398 kg/mm<sup>2</sup> [56]. Lastly, the NaAlO<sub>2</sub> pattern revealed the presence of CaMgP<sub>2</sub>O<sub>7</sub>. The chemical equations representing the phases above are provided in Formulas (3)–(5).

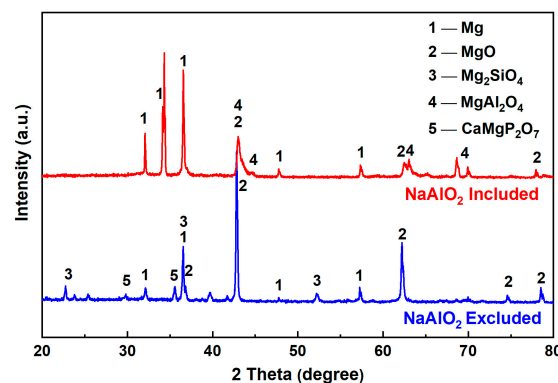


**Figure 11.** XRD patterns of 6 g/L NaAlO<sub>2</sub> coating and NaAlO<sub>2</sub> excluding the MAO coating.

Figure 12 presents the XPS analysis outcomes for MAO coatings crafted with varying concentrations of NaAlO<sub>2</sub>. The comprehensive spectrum (Figure 12a) revealed distinctive

features, and the Mg 1s spectrum showcased a fitting peak at 1303.4 eV (Figure 12b), affirming the presence of Mg; another peak at 1303.8 eV indicated the presence of MgO. The third peak, which was at 1301 eV, stood for the  $\text{CaMgP}_2\text{O}_7$ . Finally, the peak at 1305.2 eV represented the  $\text{MgAl}_2\text{O}_4$ . This result was coherent with the XRD analyses results. They collectively confirmed the presence of MgO,  $\text{MgAl}_2\text{O}_4$ , and  $\text{CaMgP}_2\text{O}_7$  in the prepared MAO coating. Previous studies indicate that certain phases enhance corrosion resistance by forming a protective layer that seals micropores and microcracks in the primary MAO coating, such as hydroxyl apatite [28,57,58].

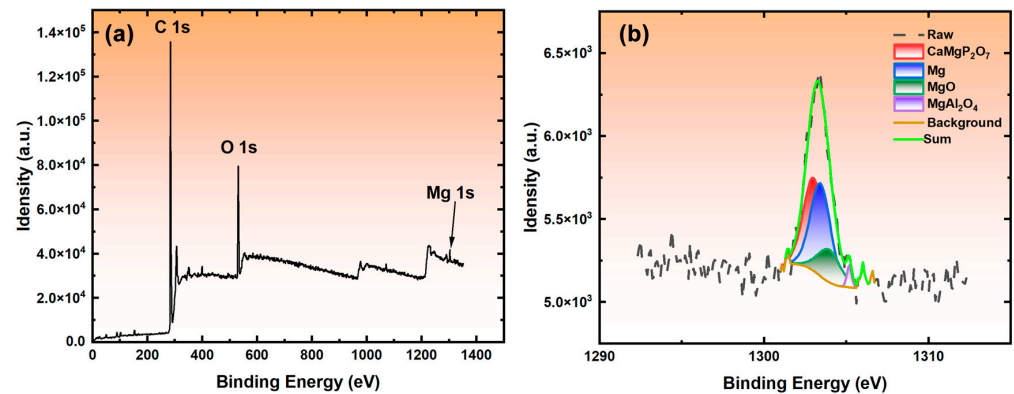


**Figure 12.** XPS analysis of Al-containing MAO coating: (a) whole spectrum; (b) Mg 1s.

Figure 13 illustrates the EDS image of four groups of MAO coatings, showing the elemental distribution across the coating cross-sections. Firstly, the Mg substrate (highlighted in red) was present in all coatings, and its proportion diminished with increasing  $\text{NaAlO}_2$  concentrations due to augmented coating thickness. The Ca element (indicated in dark green in the third column) are found in the regions with fewer defects undergoing growth. Conversely, the proportion of Al increased proportionally with the  $\text{NaAlO}_2$  concentration.

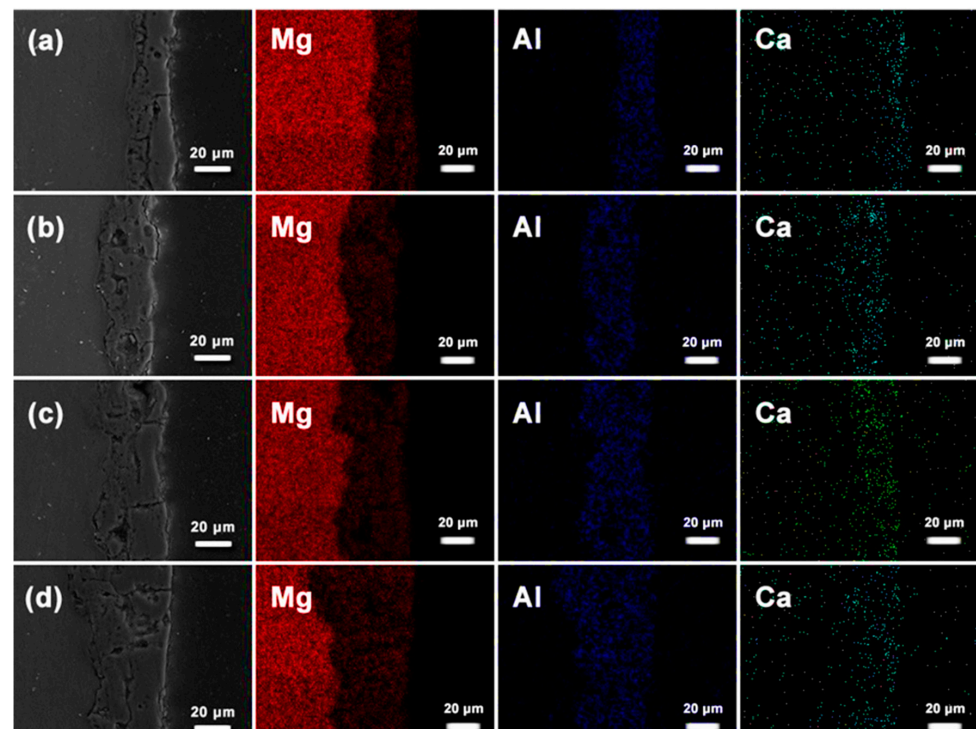


**Figure 13.** EDS image of the MAO coatings prepared with different  $\text{NaAlO}_2$  concentrations: (a) 3 g/L; (b) 6 g/L; (c) 9 g/L; (d) 12 g/L.

Table 10 details the elemental composition in the MAO coatings prepared with different NaAlO<sub>2</sub> concentrations. Higher NaAlO<sub>2</sub> concentrations corresponded to substantial increases in Ca and P elements. The Ca/P ratio, which is associated with osseous inducibility, reached a rather high value of 0.85 in the 6 g/L group and 0.92 in the 9 g/L group. This progression indicates the presence of high-temperature phases like MgAl<sub>2</sub>O<sub>4</sub> and CaMgP<sub>2</sub>O<sub>7</sub> in the MAO coating. Incorporating Ca and P elements in the MAO coating enhances adhesion forces and improves biocompatibility, as supported by previous studies [59,60].

**Table 10.** Element composition of the MAO coatings prepared with different NaAlO<sub>2</sub> concentrations (at%).

NaAlO <sub>2</sub> Concentration (g/L)	Mg	Al	Si	P	Ca	Ca/P
3	56.14	16.50	14.45	7.76	5.14	0.66
6	51.33	21.16	12.02	8.34	7.15	0.85
9	44.61	22.30	8.05	13.00	12.04	0.92
12	39.96	24.16	4.29	17.78	13.81	0.78

### 3.5. Influence of NaAlO<sub>2</sub> Concentration on the Corrosion Behavior

In this section, each experimental group comprised four parallel samples designated for immersion tests spanning 5, 10, 15, and 20 days in Hank's solution. The immersion medium employed was Hank's balanced salt solution, with regular refreshing every 24 h to maintain consistent testing conditions.

Figure 14 presents the average corrosion rates of the MAO coatings across different groups. After 5 days of immersion, the 6 g/L group exhibited a corrosion rate below 0.25 mg/(cm<sup>2</sup>·d), while the 12 g/L group experienced a slightly higher corrosion rate at 0.37 mg/(cm<sup>2</sup>·d). Over time, the corrosion rates in all groups gradually decreased, with the 6 g/L group consistently maintaining the lowest level. Despite the proximity of corrosion rates in the 3 g/L and 9 g/L groups, notable differences in thickness and porosity were observed. The MAO coating thickness in the 9 g/L group was almost twice that in the 3 g/L group, while its porosity was 12.4% compared to 10.5% in the 3 g/L group. This finding implies that higher porosity, which leads to more channels for the corrosive solution to reach the Mg alloy substrate, would significantly impact corrosion resistance more than coating thickness does. Therefore, coatings with lower porosity and better uniformity may possess stronger corrosion resistance. In this study, the MAO coating prepared with 6 g/L NaAlO<sub>2</sub> aligned most closely with this criterion, being consistent with the test results. Other research corroborates that modifying the concentration of a single electrolyte ingredient can enhance the compactness; surface quality; and, consequently, the corrosion resistance of MAO coatings [61–63].

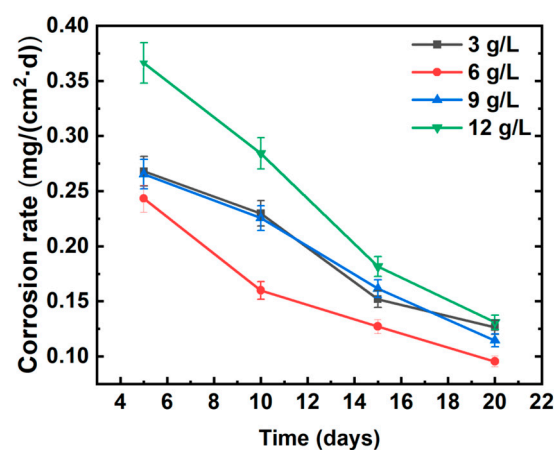


**Figure 14.** The average corrosion rate of the MAO coatings of 3, 6, 9, and 12 g/L NaAlO<sub>2</sub> concentrations.

The equivalent electrical circuit (EEC) is presented in Figure 15. In the circumstances of this paper,  $R_1$  stands for the electrolyte solution resistance,  $R_2$  is the charge transfer resistance,  $R_3$  represents the coating resistance, and  $R_4$  together with  $L$  are used to describe the resistance and inductance of pores in coating.  $CPE_1$ , which stands for constant phase element, represents the capacitance behavior of coating-substrate interface in this paper [64,65]. The impedance of CPE can be defined as Formula (6), being applied usually in a non-uniform system, which is apparently coherent with the circumstance of this paper, with  $C_1$  being the capacitance of the coating surface.

$$Z_{CPE} = \frac{1}{Q(j\omega)^n} \tag{6}$$

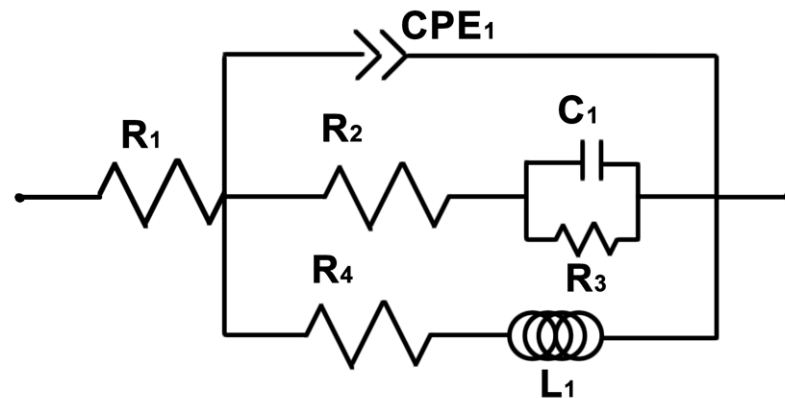


Figure 15. Equivalent electrical circuit of the EIS test.

In the equation,  $Q$  represents the constant associated with CPE,  $\omega$  denotes the angular frequency (in rad/s),  $j$  signifies the imaginary unit where  $j^2$  equals  $-1$ , and  $n$  stands for the CPE exponent.

The electrochemical results are presented in Figure 16. The Nyquist plotting shows the impedance of MAO coating (Figure 17a). Statistic fitting results are shown in Table 11.

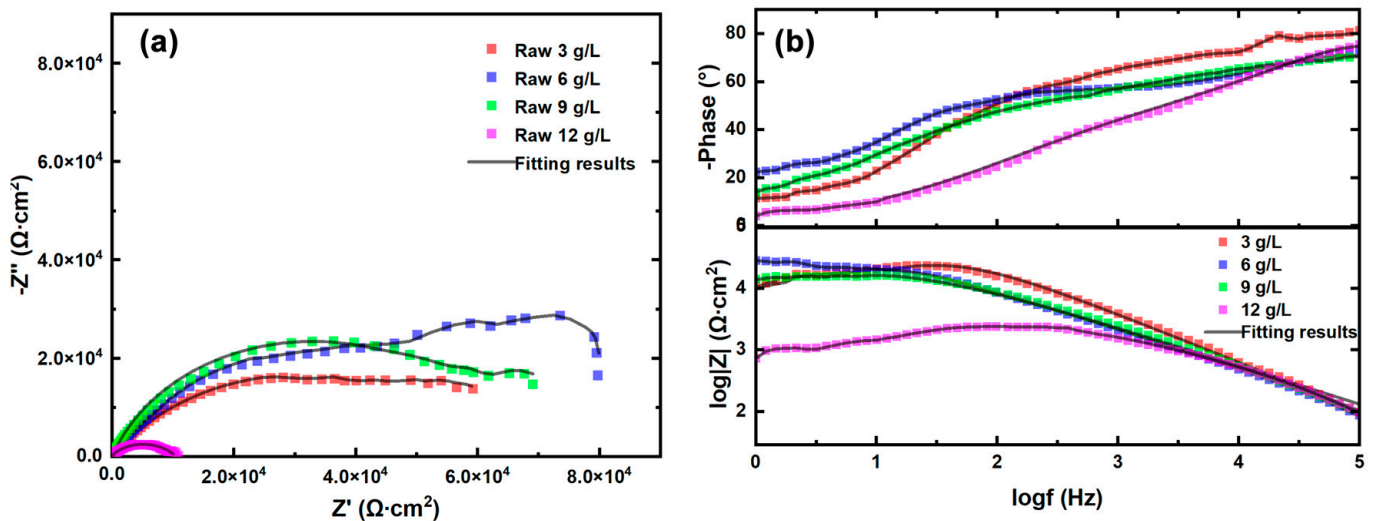
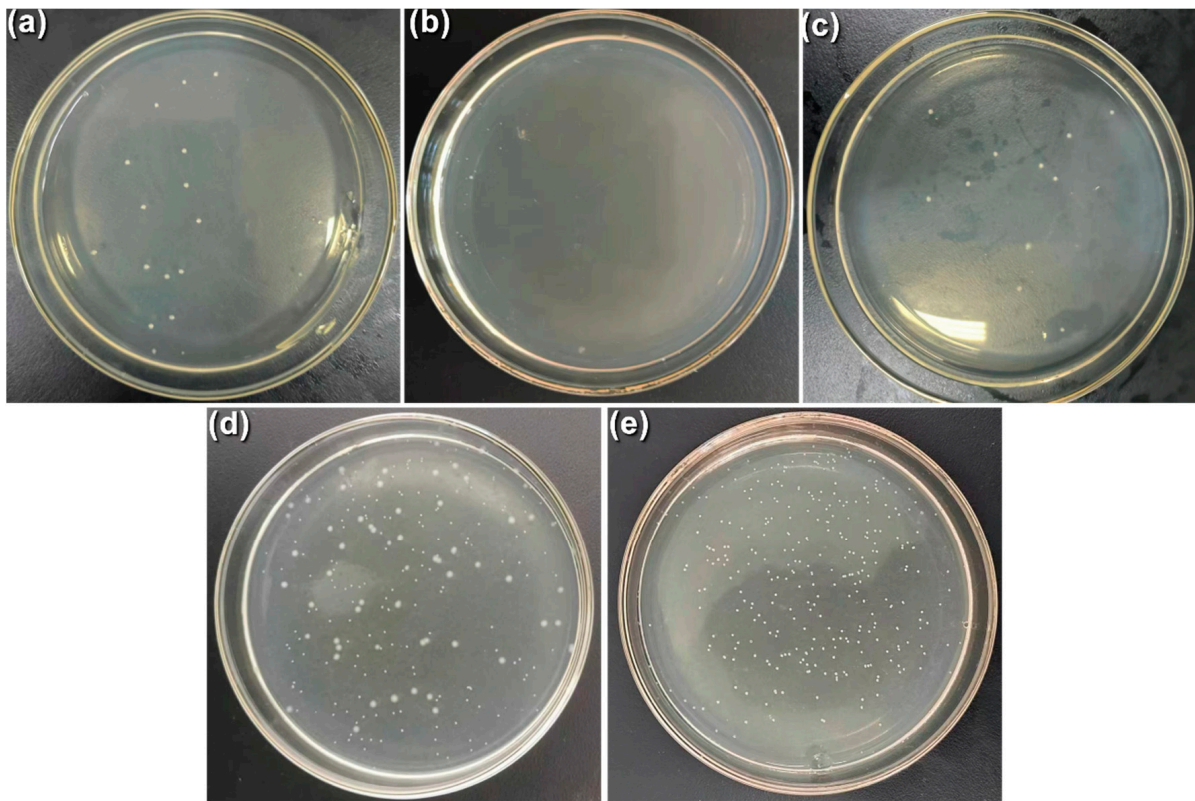


Figure 16. Fitting results of corrosion tests: (a) Nyquist plotting; (b) Bode plotting.



**Figure 17.** Anti-bacterial test results of the MAO coatings prepared with different NaAlO<sub>2</sub> concentrations: (a) 3 g/L; (b) 6 g/L; (c) 9 g/L; (d) 12 g/L; (e) control.

**Table 11.** Fitting impedance of the MAO coatings.

NaAlO <sub>2</sub> Concentration (g/L)	R <sub>1</sub> (Ω·cm <sup>2</sup> )	CPE <sub>1</sub>		R <sub>2</sub> (Ω·cm <sup>2</sup> )	R <sub>3</sub> (Ω·cm <sup>2</sup> )	C <sub>1</sub> (F × cm <sup>-2</sup> )	R <sub>4</sub> (Ω·cm <sup>2</sup> )	L (H·cm <sup>2</sup> )	χ <sup>2</sup>
		Q (Ω <sup>-1</sup> ·cm <sup>-2</sup> ·s <sup>n</sup> )	n						
3	15 ± 0.82	3.22 ± 0.47 × 10 <sup>-6</sup>	0.82 ± 0.02	4.2 ± 0.17 × 10 <sup>4</sup>	4.27 ± 0.23 × 10 <sup>4</sup>	3.1 × 10 <sup>-4</sup>	3.08 ± 0.23 × 10 <sup>4</sup>	4.36 ± 0.31 × 10 <sup>4</sup>	1.15 × 10 <sup>-4</sup>
6	12 ± 1.11	3.48 ± 0.53 × 10 <sup>-6</sup>	0.85 ± 0.01	4.0 ± 0.23 × 10 <sup>4</sup>	8.14 ± 0.37 × 10 <sup>4</sup>	4.3 × 10 <sup>-4</sup>	6.32 ± 0.21 × 10 <sup>4</sup>	5.82 ± 0.33 × 10 <sup>4</sup>	1.03 × 10 <sup>-4</sup>
9	11 ± 1.31	2.46 ± 0.35 × 10 <sup>-6</sup>	0.80 ± 0.02	4.4 ± 0.29 × 10 <sup>4</sup>	6.6 ± 0.31 × 10 <sup>4</sup>	4.9 × 10 <sup>-4</sup>	2.1 ± 0.11 × 10 <sup>4</sup>	3.4 ± 0.07 × 10 <sup>4</sup>	1.68 × 10 <sup>-4</sup>
12	10 ± 0.97	1.53 ± 0.17 × 10 <sup>-6</sup>	0.79 ± 0.02	4.1 ± 0.22 × 10 <sup>4</sup>	1.7 ± 0.27 × 10 <sup>4</sup>	4.8 × 10 <sup>-4</sup>	0.9 ± 0.02 × 10 <sup>4</sup>	0.97 ± 0.01 × 10 <sup>4</sup>	1.33 × 10 <sup>-4</sup>

Taking into consideration both surface and cross-sectional morphologies, alterations in coating thickness and coating compactness indicate the evolution of impedance. With an escalation in the concentration of NaAlO<sub>2</sub> in the electrolyte, the coating thickened with a concomitant decline in coating uniformity, flatness, and perfectness.

The fitting results delineated in Table 11 and Figure 16 elucidate that R<sub>1</sub>, the impedance of the electrolyte solution, remained relatively stable at 10–15 Ω·cm<sup>2</sup>, with a tiny decline due to the increased concentrations of the electrolyte. R<sub>2</sub> was also stable at about 4 × 10<sup>4</sup> Ω·cm<sup>2</sup> because it related directly with temperature T and exchange current i<sub>0</sub>. R<sub>3</sub>, which represents the resistance of the MAO coating, differed significantly in each group, rising with the introduction of NaAlO<sub>2</sub> at the beginning, then peaking in the 6 g/L group with the impedance of 8.14 × 10<sup>4</sup> Ω·cm<sup>2</sup>, and finally declining to 1.7 × 10<sup>4</sup> Ω·cm<sup>2</sup> in the 12 g/L group. R<sub>4</sub> and L, which are related to the resistance and inductance of pores in MAO coatings, showed synchronized evolvment with coating compactness. They firstly rose with the introduction of NaAlO<sub>2</sub> in electrolytes; peaked at 6.32 × 10<sup>4</sup> Ω·cm<sup>2</sup> and 5.82 × 10<sup>4</sup> H·cm<sup>2</sup>, respectively, in the 6 g/L group, which possessed the least pores and cracks, etc.; and then declined with when NaAlO<sub>2</sub> was overdosed in electrolytes, in the 9 and 12 g/L groups. On the other hand, CPE<sub>1</sub> and R<sub>2</sub>, associated with the outer porous layer, peaked in the 6 g/L group and declined with higher NaAlO<sub>2</sub> concentration, but the impedance of 9 g/L was still considerably higher than those of the 3 and 12 g/L groups.

Though the resistances  $R_1$ ,  $R_2$ ,  $R_3$ , and  $R_4$  cannot be simply summed together, it can be concluded from the results that the MAO coating in the 6 g/L group possessed higher impedance, in other words, better corrosion resistance. The results can be related to the coating's thickness and perfectness. The MAO coating in the 6 g/L group, though having lower thickness compared to the coating in the 9 and 12 g/L groups, also possessed much less pores and cracks, providing easy access for corrosive medium to Mg substrate, severely damaging the corrosion resistance of a coating. In other studies, where bare ZK60 alloy subjected to EIS testing in Hank's solution demonstrated an impedance of approximately  $1000 \Omega \cdot \text{cm}^2$  at  $37^\circ \text{C}$  [66]. It can be seen that the MAO coating significantly improved the corrosion resistance.

### 3.6. Influence of $\text{NaAlO}_2$ Concentration on the Antibacterial Behavior of MAO Coating

This section investigates and discusses the antibacterial ability of the MAO coating and the influence of  $\text{NaAlO}_2$  concentration on it. Since the antibacterial test provided qualitative data, it offers evidence for a comparative analysis of the antibacterial capabilities of MAO coatings prepared with varying  $\text{NaAlO}_2$  concentrations.

Figure 17 displays the results of the antibacterial ability test for MAO coatings in four groups. The figure reveals a significantly higher number of bacterial colonies in the 12 g/L group (Figure 18d), indicating a comparatively weaker antibacterial ability in this group. In the 3 g/L group, large bacterial colonies were observed. The 6 g/L group exhibited nine small colonies, while the 9 g/L group displayed twelve large colonies. The 12 g/L group substantially increased with 45 large colonies. The control group (Figure 17e) had 309 bacterial colonies. Consequently, the antibacterial rate ( $R_{ab}$ ), calculated using Formula (7), quantitatively measured the antibacterial ability.

$$R_{ab} = \frac{|N_x - N_c|}{N_c} \quad (7)$$

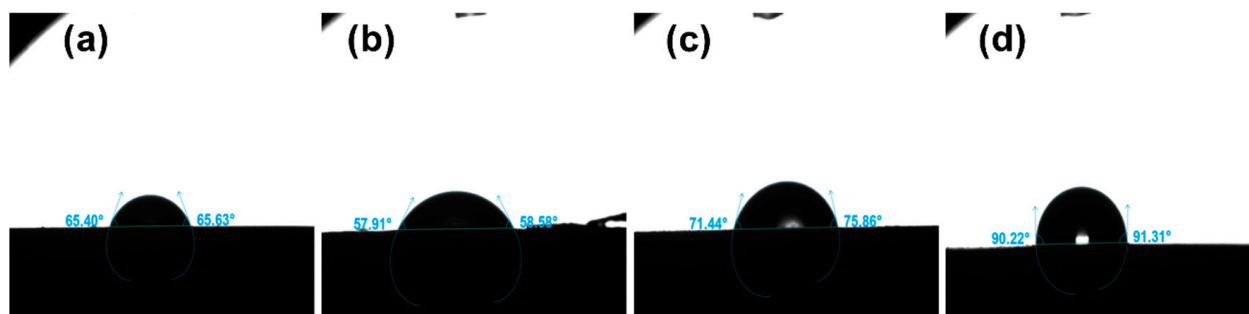


**Figure 18.** Water contact angles of the MAO coatings prepared with different  $\text{NaAlO}_2$  concentrations: (a) 3 g/L; (b) 6 g/L; (c) 9 g/L; (d) 12 g/L.

In this formula,  $N_x$  represents the numbers of bacterial colonies in the four groups, while  $N_c$  denotes the number of bacterial colonies in the control group. Consequently, the calculated antibacterial rates  $R_{ab}$  were 95.47%, 97.08%, 96.11%, and 85.4% for the respective groups.

### 3.7. Influence of $\text{NaAlO}_2$ Concentration on the Water Contact Angles of MAO Coatings

One method used to characterize the hydrophilicity of a biomedical material is the measurement of the water contact angle. Figure 18 illustrates the water contact angle results for MAO coatings prepared with different  $\text{NaAlO}_2$  concentrations. The water contact angles of the MAO coatings were automatically calculated and marked by the software. The results indicate that as the  $\text{NaAlO}_2$  concentration in the electrolyte increased, the water contact angle of the MAO coating initially decreased before subsequent elevation. The MAO coating in the 6 g/L  $\text{NaAlO}_2$  group exhibited the lowest water contact angle,

suggesting superior biocompatibility compared to other groups. This finding implies minimal difficulty for cell attachment on the coating surface.

#### 4. Conclusions

In this study, coatings with different NaAlO<sub>2</sub> concentrations in electrolytes were successfully fabricated on ZK60 magnesium alloy substrates. The following conclusions can be drawn from the comprehensive tests and analyses conducted:

1. MAO coating prepared with 6 g/L NaAlO<sub>2</sub> exhibited desired properties characterized by enough thickness, compactness, and at least better uniformity than other groups. Phase composition, including MgAl<sub>2</sub>O<sub>4</sub> and CaMgP<sub>2</sub>O<sub>7</sub> obtained from XRD, XPS, and EDS analyses, were consistent, confirming the presence of Mg<sub>2</sub>SiO<sub>4</sub>, MgAlO<sub>4</sub>, and CaMgP<sub>2</sub>O<sub>7</sub>, together with Mg and MgO phases.
2. The concentration of NaAlO<sub>2</sub> significantly influenced coating properties by altering the electrical conductance and the voltage values during preparation. Higher concentrations, such as 9 g/L and 12 g/L NaAlO<sub>2</sub>, resulted in a more intense reaction, leading to increased thickness and defects, as well as diminished compactness in the MAO coating. These drawbacks were evident in the microstructure, cross-sectional morphology, and mechanical properties such as hardness and wear resistance. The hardness of the 6 g/L group was the highest, at 411.2 HV.
3. The water contact angle test revealed that the coating from the 6 g/L group had the lowest water contact angle (58.25°), indicating the best hydrophilicity. The fitting impedance of the MAO coating in the 6 g/L group was the highest coating resistance R<sub>3</sub> (8.14 × 10<sup>4</sup> Ω·cm<sup>2</sup>) compared to other groups, attributable to its minimal pores and cracks. These defects are crucial as conductive channels when exposed to external corrosive medium.

**Author Contributions:** Conceptualization, Z.-X.W., S.L. and L.-Y.C.; methodology, W.-G.L., Z.-X.W., J.-J.G. and S.L.; software, J.-J.G., S.-F.Z., J.-W.Z. and D.O.; validation, Z.-X.W., L.-Y.C. and S.L.; formal analysis, J.-J.G., J.-W.Z. and S.-F.Z.; data curation, Z.-X.W., J.-W.Z. and W.-G.L.; writing—original draft preparation, S.-F.Z., Z.-X.W. and L.-Y.C.; writing—review and editing, Z.-X.W., L.-Y.C., D.O. and S.L.; visualization, S.-F.Z.; supervision, Z.-X.W. and W.-G.L.; project administration, S.L., J.-W.Z. and D.O. All authors have read and agreed to the published version of the manuscript.

**Funding:** This research received no external funding.

**Institutional Review Board Statement:** Not applicable.

**Informed Consent Statement:** Not applicable.

**Data Availability Statement:** Data are contained within the article.

**Conflicts of Interest:** The authors declare no conflicts of interest.

#### References

1. Hench, L.L.; Polak, J.M. Third-generation biomedical materials. *Science* **2002**, *295*, 1014–1017. [[CrossRef](#)] [[PubMed](#)]
2. Narayan, R. *Biomedical Materials*; Springer: Berlin/Heidelberg, Germany, 2009; Volume 1.
3. Nikolova, M.P.; Chavali, M.S. Metal oxide nanoparticles as biomedical materials. *Biomimetics* **2020**, *5*, 27. [[CrossRef](#)] [[PubMed](#)]
4. Ibrahim, M.Z.; Sarhan, A.A.; Yusuf, F.; Hamdi, M. Biomedical materials and techniques to improve the tribological, mechanical and biomedical properties of orthopedic implants—A review article. *J. Alloys Compd.* **2017**, *714*, 636–667. [[CrossRef](#)]
5. Chen, L.-Y.; Liang, S.-X.; Liu, Y.; Zhang, L.-C. Additive manufacturing of metallic lattice structures: Unconstrained design, accurate fabrication, fascinated performances, and challenges. *Mater. Sci. Eng. R Rep.* **2021**, *146*, 100648. [[CrossRef](#)]
6. Kobayashi, E.; Matsumoto, S.; Doi, H.; Yoneyama, T.; Hamanaka, H. Mechanical properties of the binary titanium-zirconium alloys and their potential for biomedical materials. *J. Biomed. Mater. Res.* **1995**, *29*, 943–950. [[CrossRef](#)]
7. Bullock, C.J.; Bussy, C. Biocompatibility considerations in the design of graphene biomedical materials. *Adv. Mater. Interfaces* **2019**, *6*, 1900229. [[CrossRef](#)]
8. Li, H.; Yan, Y.-G.; Wei, J.; Ma, J.; Gong, M.; Luo, X.-M.; Zhang, Y.-F. Bone substitute biomedical material of multi-(amino acid) copolymer: In vitro degradation and biocompatibility. *J. Mater. Sci. Mater. Med.* **2011**, *22*, 2555–2563. [[CrossRef](#)]

9. Ornberg, A.; Pan, J.-S.; Herstedt, M.; Leygraf, C. Corrosion resistance, chemical passivation, and metal release of 35N LT and MP35N for biomedical material application. *J. Electrochem. Soc.* **2007**, *154*, C546. [[CrossRef](#)]
10. Tavares, A.; Fernandes, B.; Souza, S.; Batista, W.; Cunha, F.; Landers, R.; Macedo, M. The addition of Si to the Ti-35Nb alloy and its effect on the corrosion resistance, when applied to biomedical materials. *J. Alloys Compd.* **2014**, *591*, 91–99. [[CrossRef](#)]
11. Cui, Y.-W.; Chen, L.-Y.; Qin, P.; Li, R.; Zang, Q.; Peng, J.; Zhang, L.; Lu, S.; Wang, L.; Zhang, L.-C. Metastable pitting corrosion behavior of laser powder bed fusion produced Ti-6Al-4V in Hank's solution. *Corros. Sci.* **2022**, *203*, 110333. [[CrossRef](#)]
12. Gu, Z.; Thomas, A.C.; Xu, Z.-P.; Campbell, J.H.; Lu, G.-Q. In vitro sustained release of LMWH from MgAl-layered double hydroxide nano hybrids. *Chem. Mater.* **2008**, *20*, 3715–3722. [[CrossRef](#)]
13. Tang, E.S.; Chan, L.-W.; Heng, P.W. Coating of multiparticulates for sustained release. *Am. J. Adv. Drug Deliv.* **2005**, *3*, 17–28. [[CrossRef](#)]
14. Bamberger, M.; Dehm, G. Trends in the development of new Mg alloys. *Annu. Rev. Mater. Res.* **2008**, *38*, 505–533. [[CrossRef](#)]
15. Li, N.; Zheng, Y.-F. Novel magnesium alloys developed for biomedical application: A review. *J. Mater. Sci. Technol.* **2013**, *29*, 489–502. [[CrossRef](#)]
16. Rahman, M.; Li, Y.-C.; Wen, C.-E. HA coating on Mg alloys for biomedical applications: A review. *J. Magnes. Alloys* **2020**, *8*, 929–943. [[CrossRef](#)]
17. Raffa, M.L.; Nguyen, V.H.; Hernigou, P.; Flouzat-Lachaniette, C.H.; Haiat, G. Stress shielding at the bone-implant interface: Influence of surface roughness and of the bone-implant contact ratio. *J. Orthop. Res.* **2021**, *39*, 1174–1183. [[CrossRef](#)]
18. Pan, F.-S.; Yang, M.-B.; Chen, X.-H. A review on casting magnesium alloys: Modification of commercial alloys and development of new alloys. *J. Mater. Sci. Technol.* **2016**, *32*, 1211–1221. [[CrossRef](#)]
19. Pak, S.-N.; Yao, Z.-P.; Ju, K.-S.; Ri, C.-N.; Xia, Q.-X. Effect of organic additives on structure and corrosion resistance of MAO coating. *Vacuum* **2018**, *151*, 8–14. [[CrossRef](#)]
20. Shi, L.-L.; Xu, Y.-J.; Li, K.; Yao, Z.-P.; Wu, S.-Q. Effect of additives on structure and corrosion resistance of ceramic coatings on Mg-Li alloy by micro-arc oxidation. *Curr. Appl. Phys.* **2010**, *10*, 719–723. [[CrossRef](#)]
21. Shao, L.-L.; Li, H.-T.; Jiang, B.-L.; Liu, C.-C.; Gu, X.; Chen, D.-C. A comparative study of corrosion behavior of hard anodized and micro-arc oxidation coatings on 7050 aluminum alloy. *Metals* **2018**, *8*, 165. [[CrossRef](#)]
22. Xu, C.; Chen, L.-Y.; Zheng, C.-B.; Zhang, Z.-Y.; Li, R.-F.; Yang, H.-Y.; Peng, J.-H.; Zhang, L.-N.; Zhang, L.-C. Bioactive Performances of Surface Modification of Ti-6Al-4V Jointly Using Ultrasonic-Assisted Microarc Oxidation and Hydrothermal Treatment. *Adv. Eng. Mater.* **2022**, *24*, 2200674. [[CrossRef](#)]
23. Zhang, L.; Zhang, J.-Q.; Chen, C.-F.; Gu, Y.-H. Advances in microarc oxidation coated AZ31 Mg alloys for biomedical applications. *Corros. Sci.* **2015**, *91*, 7–28. [[CrossRef](#)]
24. Chang, L.-R.; Cao, F.-H.; Cai, J.-S.; Liu, W.-J.; Zhang, Z.; Zhang, J.-Q. Influence of electric parameters on MAO of AZ91D magnesium alloy using alternative square-wave power source. *Trans. Nonferrous Met. Soc. China* **2011**, *21*, 307–316. [[CrossRef](#)]
25. Liu, H.; Gao, S.-W.; Cai, J.-S.; He, C.-L.; Mao, J.-J.; Zhu, T.-X.; Chen, Z.; Huang, J.-Y.; Meng, K.; Zhang, K.-Q. Recent progress in fabrication and applications of superhydrophobic coating on cellulose-based substrates. *Materials* **2016**, *9*, 124. [[CrossRef](#)]
26. Zhang, R.-F.; Xiong, G.-Y.; Hu, C.-Y. Comparison of coating properties obtained by MAO on magnesium alloys in silicate and phytic acid electrolytes. *Curr. Appl. Phys.* **2010**, *10*, 255–259. [[CrossRef](#)]
27. Liang, J.; Guo, B.-G.; Tian, J.; Liu, H.-W.; Zhou, J.-F.; Liu, W.-M.; Xu, T. Effects of NaAlO<sub>2</sub> on structure and corrosion resistance of microarc oxidation coatings formed on AM60B magnesium alloy in phosphate-KOH electrolyte. *Surf. Coat. Technol.* **2005**, *199*, 121–126. [[CrossRef](#)]
28. Feng, Y.-S.; Ma, X.; Chang, L.; Zhu, S.-J.; Guan, S.-K. Characterization and cytocompatibility of polydopamine on MAO-HA coating supported on Mg-Zn-Ca alloy. *Surf. Interface Anal.* **2017**, *49*, 1115–1123. [[CrossRef](#)]
29. Sun, J.-f.; Han, Y.; Huang, X. Hydroxyapatite coatings prepared by micro-arc oxidation in Ca-and P-containing electrolyte. *Surf. Coat. Technol.* **2007**, *201*, 5655–5658. [[CrossRef](#)]
30. Qiao, Y.-X.; Qin, Y.; Zhou, H.-L.; Yang, L.-L.; Wang, X.-J.; Wang, Z.-B.; Liu, Z.-G.; Zou, J.-S. Electrochemical Hydrogen Charging on Corrosion Behavior of Ti-6Al-4V Alloy in Artificial Seawater. *Chin. J. Mech. Eng.* **2024**, *37*, 2. [[CrossRef](#)]
31. Zou, Z.; Liu, Z.-H.; Yang, L.-L.; Tang, Y.-B.; Qiao, Y.-X.; Lu, D.-H. Corrosion behavior of different building planes of selective laser melting 316L stainless steel in 0.1 M HCl solution. *J. Mater. Res. Technol.* **2024**, *28*, 4738–4753. [[CrossRef](#)]
32. He, X.-J.; Zhang, X.-Y.; Wang, X.; Qin, L. Review of antibacterial activity of titanium-based implants' surfaces fabricated by micro-arc oxidation. *Coatings* **2017**, *7*, 45. [[CrossRef](#)]
33. Tian, Y.-X.; Cao, H.-L.; Qiao, Y.-Q.; Meng, F.-H.; Liu, X.-Y. Antibacterial activity and cytocompatibility of titanium oxide coating modified by iron ion implantation. *Acta Biomater.* **2014**, *10*, 4505–4517. [[CrossRef](#)] [[PubMed](#)]
34. He, X.-J.; Zhang, G.-N.; Wang, X.; Hang, R.-Q.; Huang, X.-B.; Qin, L.; Tang, B.; Zhang, X.-Y. Biocompatibility, corrosion resistance and antibacterial activity of TiO<sub>2</sub>/CuO coating on titanium. *Ceram. Int.* **2017**, *43*, 16185–16195. [[CrossRef](#)]
35. Lin, Z.-S.; Sun, X.-T.; Yang, H.-Z. The role of antibacterial metallic elements in simultaneously improving the corrosion resistance and antibacterial activity of magnesium alloys. *Mater. Des.* **2021**, *198*, 109350. [[CrossRef](#)]
36. Li, J.-H.; Fu, J.-M.; Tian, X.; Hua, T.; Poon, T.-Y.; Koo, M.-K.; Chan, W.-M. Characteristics of chitosan fiber and their effects towards improvement of antibacterial activity. *Carbohydr. Polym.* **2022**, *280*, 119031. [[CrossRef](#)] [[PubMed](#)]

37. Bakhsheshi-Rad, H.; Hamzah, E.; Ismail, A.; Aziz, M.; Daroonparvar, M.; Saebnoori, E.; Chami, A. In vitro degradation behavior, antibacterial activity and cytotoxicity of TiO<sub>2</sub>-MAO/ZnHA composite coating on Mg alloy for orthopedic implants. *Surf. Coat. Technol.* **2018**, *334*, 450–460. [[CrossRef](#)]
38. Xue, K.; Liang, L.-X.; Cheng, S.-C.; Liu, H.-P.; Cui, L.-Y.; Zeng, R.-C.; Li, S.-Q.; Wang, Z.-L. Corrosion resistance, antibacterial activity and drug release of ciprofloxacin-loaded micro-arc oxidation/silane coating on magnesium alloy AZ31. *Prog. Org. Coat.* **2021**, *158*, 106357. [[CrossRef](#)]
39. Wang, Z.-X.; Chen, G.-Q.; Chen, L.-Y.; Xu, L.; Lu, S. Degradation behavior of micro-arc oxidized ZK60 magnesium alloy in a simulated body fluid. *Metals* **2018**, *8*, 724. [[CrossRef](#)]
40. Coates, G. 124. The standard electrode potential of magnesium. *J. Chem. Soc.* **1945**, 478–479. [[CrossRef](#)]
41. Fernandez-Prini, R. Conductance of electrolyte solutions. A modified expression for its concentration dependence. *Trans. Faraday Soc.* **1969**, *65*, 3311–3313. [[CrossRef](#)]
42. Kirkwood, J.G. On the theory of strong electrolyte solutions. *J. Chem. Phys.* **1934**, *2*, 767–781. [[CrossRef](#)]
43. Han, I.-H.; Choi, J.-H.; Zhao, B.-H.; Baik, H.-K.; Lee, I.-S. Micro-arc oxidation in various concentration of KOH and structural change by different cut off potential. *Curr. Appl. Phys.* **2007**, *7*, e23–e27. [[CrossRef](#)]
44. Wang, Z.-Y.; Ma, Y.; Wang, Y.-S. Effect of V<sub>2</sub>O<sub>5</sub> Additive on Micro-Arc Oxidation Coatings Fabricated on Magnesium Alloys with Different Loading Voltages. *Metals* **2020**, *10*, 1146. [[CrossRef](#)]
45. Wang, Z.-X.; Zhang, J.-W.; Lv, W.-G.; Chen, L.-Y.; Qi, F.; Chen, W.-W.; Lu, S. Growth Mechanism of Ceramic Coating on ZK60 Magnesium Alloy Based on Two-Step Current-Decreasing Mode of Micro-Arc Oxidation. *Adv. Eng. Mater.* **2022**, *24*, 2101232. [[CrossRef](#)]
46. Cui, L.-Y.; Zeng, R.-C.; Guan, S.-K.; Qi, W.-C.; Zhang, F.; Li, S.-Q.; Han, E.-H. Degradation mechanism of micro-arc oxidation coatings on biodegradable Mg-Ca alloys: The influence of porosity. *J. Alloys Compd.* **2017**, *695*, 2464–2476. [[CrossRef](#)]
47. Chen, J.; Wang, Z.-X.; Lu, S. Effects of electric parameters on microstructure and properties of MAO coating fabricated on ZK60 Mg alloy in dual electrolyte. *Rare Metals* **2012**, *31*, 172–177. [[CrossRef](#)]
48. Narayanan, T.S.; Park, I.S.; Lee, M.-H. Strategies to improve the corrosion resistance of microarc oxidation (MAO) coated magnesium alloys for degradable implants: Prospects and challenges. *Prog. Mater. Sci.* **2014**, *60*, 1–71. [[CrossRef](#)]
49. Vitosytė, J.; Ukvalbergienė, K.; Keturakis, G. The effects of surface roughness on adhesion strength of coated ash (*Fraxinus excelsior* L.) and birch (*Betula* L.) wood. *Mater. Sci.* **2012**, *18*, 347–351. [[CrossRef](#)]
50. Darband, G.B.; Aliofkhaezrai, M.; Hamghalam, P.; Valizade, N. Plasma electrolytic oxidation of magnesium and its alloys: Mechanism, properties and applications. *J. Magnes. Alloy* **2017**, *5*, 74–132. [[CrossRef](#)]
51. Xu, C.; Chen, L.-Y.; Zheng, C.-B.; Zhang, H.-Y.; Zhao, C.-H.; Wang, Z.-X.; Lu, S.; Zhang, J.-W.; Zhang, L.-C. Improved wear and corrosion resistance of microarc oxidation coatings on Ti-6Al-4V alloy with ultrasonic assistance for potential biomedical applications. *Adv. Eng. Mater.* **2021**, *23*, 2001433. [[CrossRef](#)]
52. Lin, X.; Wang, X.; Tan, L.; Wan, P.; Yu, X.-M.; Li, Q.; Yang, K. Effect of preparation parameters on the properties of hydroxyapatite containing micro-arc oxidation coating on biodegradable ZK60 magnesium alloy. *Ceram. Int.* **2014**, *40*, 10043–10051. [[CrossRef](#)]
53. Zhang, R.-F.; Lv, K.; Du, Z.-X.; Chen, W.-D.; Ji, P.-F.; Wang, M.-L. Effects of graphene on the wear and corrosion resistance of micro-arc oxidation coating on a titanium alloy. *Metals* **2021**, *12*, 70. [[CrossRef](#)]
54. Moore, P.B.; Smith, J.V. High pressure modification of Mg<sub>2</sub>SiO<sub>4</sub>: Crystal structure and crystallochemical and geophysical implications. *Nature* **1969**, *221*, 653–655. [[CrossRef](#)]
55. Horoshavin, L. *Spinel Nano-Refractory Materials*; UB RAS: Ekaterinburg, Russia, 2009; p. 600.
56. Shi, Z.-Q.; Zhao, Q.-L.; Guo, B.; Ji, T.-Y.; Wang, H. A review on processing polycrystalline magnesium aluminate spinel (MgAl<sub>2</sub>O<sub>4</sub>): Sintering techniques, material properties and machinability. *Mater. Des.* **2020**, *193*, 108858. [[CrossRef](#)]
57. Dai, X.-J.; Li, X.-C.; Wang, C.; Yu, S.; Yu, Z.-T.; Yang, X.-R. Effect of MAO/Ta<sub>2</sub>O<sub>5</sub> composite coating on the corrosion behavior of Mg-Sr alloy and its in vitro biocompatibility. *J. Mater. Res. Technol.* **2022**, *20*, 4566–4575. [[CrossRef](#)]
58. Xiong, Y.; Hu, Q.; Hu, X.-X.; Song, R.-G. Microstructure and corrosion resistance of Ti<sub>3</sub>O<sub>5</sub>-HA bio-ceramic coating fabricated on AZ80 magnesium alloy. *Surf. Coat. Technol.* **2017**, *325*, 239–247. [[CrossRef](#)]
59. Yao, Z.-Q.; Ivanisenko, Y.; Diemant, T.; Caron, A.; Chuvilin, A.; Jiang, J.-Z.; Valiev, R.; Qi, M.; Fecht, H. Synthesis and properties of hydroxyapatite-containing porous titania coating on ultrafine-grained titanium by micro-arc oxidation. *Acta Biomater.* **2010**, *6*, 2816–2825. [[CrossRef](#)] [[PubMed](#)]
60. Song, W.-H.; Jun, Y.-K.; Han, Y.; Hong, S.-H. Biomimetic apatite coatings on micro-arc oxidized titania. *Biomaterials* **2004**, *25*, 3341–3349. [[CrossRef](#)]
61. Qin, Y.; Wu, G.-H.; Atrens, A.; Zhang, X.-L.; Zhang, L.; Ding, W.-J. Effect of NaOH concentration on microstructure and corrosion resistance of MAO coating on cast Al-Li alloy. *Trans. Nonferrous Met. Soc. China* **2021**, *31*, 913–924. [[CrossRef](#)]
62. Wang, S.-H.; Guo, X.-W.; Xie, Y.-J.; Liu, L.-H.; Yang, H.-Y.; Zhu, R.-Y.; Gong, J.; Peng, L.-M.; Ding, W.-J. Preparation of superhydrophobic silica film on Mg-Nd-Zn-Zr magnesium alloy with enhanced corrosion resistance by combining micro-arc oxidation and sol-gel method. *Surf. Coat. Technol.* **2012**, *213*, 192–201. [[CrossRef](#)]
63. Cui, Y.-W.; Chen, L.-Y.; Chu, Y.-H.; Zhang, L.; Li, R.; Lu, S.; Wang, L.; Zhang, L.-C. Metastable pitting corrosion behavior and characteristics of passive film of laser powder bed fusion produced Ti-6Al-4V in NaCl solutions with different concentrations. *Corros. Sci.* **2023**, *215*, 111017. [[CrossRef](#)]

64. Alves, A.; Wenger, F.; Ponthiaux, P.; Celis, J.-P.; Pinto, A.; Rocha, L.; Fernandes, J. Corrosion mechanisms in titanium oxide-based films produced by anodic treatment. *Electrochim. Acta* **2017**, *234*, 16–27. [[CrossRef](#)]
65. Wang, G.; Song, D.; Qiao, Y.; Cheng, J.; Liu, H.; Jiang, J.; Ma, A.; Ma, X. Developing super-hydrophobic and corrosion-resistant coating on magnesium-lithium alloy via one-step hydrothermal processing. *J. Magnes. Alloys* **2023**, *11*, 1422–1439. [[CrossRef](#)]
66. Chen, J.-X.; Yang, Y.; Tan, L.-L.; Ke, Y.; Misra, R.; Wang, J.-H.; Su, X.-P. In vitro degradation, wear property and biocompatibility of nano-Y<sub>2</sub>O<sub>3</sub>-containing micro-arc oxidation coating on ZK60 alloy. *Trans. Nonferrous Met. Soc. China* **2023**, *33*, 1411–1424. [[CrossRef](#)]

**Disclaimer/Publisher’s Note:** The statements, opinions and data contained in all publications are solely those of the individual author(s) and contributor(s) and not of MDPI and/or the editor(s). MDPI and/or the editor(s) disclaim responsibility for any injury to people or property resulting from any ideas, methods, instructions or products referred to in the content.